Gondwana Research 143 (2025) 91–124

Contents lists available at ScienceDirect

Gondwana Research

journal homepage: www.elsevier.com/locate/gr

EnMap hyperspectral data in geological investigations: Evaluation for lithological and hydrothermal alteration mapping in Neoproterozoic rocks

Ali Shebl [a,b], Mahmoud Abdellatif [c], Dávid Abriha [d,*], Maher Dawoud [e], Mosaad Ali Hussein Ali [f], Abdelhalim S. Mahmoud [g], Ferenc Kristály [h], Árpád Csámer [a,i]

[a] Department of Mineralogy and Geology, Faculty of Science and Technology, University of Debrecen, Egyetem tér 1, 4032 Debrecen, Hungary
[b] Department of Geology, Tanta University, 31527 Tanta, Egypt
[c] Department of Geology, South Valley University, 83523 Qena, Egypt
[d] Department of Physical Geography and Geoinformatics, Faculty of Science and Technology, University of Debrecen, Egyetem tér 1, 4032 Debrecen, Hungary
[e] Department of Geology, Faculty of Science, Menofia University, Shebin ElKoum, 32511 Egypt
[f] Department of Mining and Metallurgy Engineering, Assiut University, Assiut 71515, Egypt
[g] Fayoum University, Al-Fayoum 63514 Egypt
[h] Department of Geology and Mineral Deposits, Institute of Exploration Geosciences, 3515 Miskolc-Egyetemváros, Hungary
[i] Cosmochemistry and Cosmic Methods Research Group, University of Debrecen, Debrecen 4032, Hungary

ARTICLE INFO

Handling Editor: Li Tang

Keywords:
EnMap
Arabian Nubian Shield
Geological Mapping
Airborne geophysical data

ABSTRACT

This study conducted a rigorous evaluation of Environmental Mapping and Analysis Program (EnMap) data in geological applications, specifically focusing on lithological and hydrothermal alteration mapping. This research represents one of the earliest attempts to apply EnMap data for such purposes, and the first to integrate EnMap and airborne geophysical data for geological mapping over the entire Arabian Nubian Shield. To ensure a comprehensive appraisal, we selected a study area characterized by complex Precambrian rocks, including igneous, metamorphic, and sedimentary formations, alongside structural intricacies and hydrothermal activities. Our study utilized various image-processing techniques, including principal component analysis (PCA), Uniform Manifold Approximation and Projection (UMAP), Sequential Maximum Angle Convex Cone (SMACC) end-member analysis, and spectral resampling. These techniques successfully discriminated ophiolitic serpentinite, volcaniclastic metasediments (as part of the ophiolitic mélange matrix), metavolcanics, metagabbro-diorite, *syn*-orogenic granite, post-orogenic granite, Nubian sandstone, and Wadi deposits. Additionally, they revealed the prevalence of OH-bearing minerals and iron oxides as the primary hydrothermal alteration products within the study area. By correlating the findings with USGS spectral libraries and airborne geophysical data, we determined the efficacy of EnMap data in these applications. Our findings were further validated through multiscale observations, field investigations, petrographic analyses, and scanning electron microscopy-energy-dispersive X-ray spectroscopy (SEM-EDX). In addition to endorsing the use of the UMAP algorithm and EnMap data for future applications, this study highlights key alteration zones that could serve as potential targets for future gold exploration, alongside insights into bauxite ore occurrences.

1. Introduction

Over the last few years, significant investments have been directed towards the deployment of hyperspectral satellite systems dedicated to Earth observation and monitoring. The Environmental Mapping and Analysis Program (EnMAP), a recently launched German hyperspectral satellite, is anticipated to facilitate various environmental and geological applications through spectral enhancements compared to previous hyperspectral satellites. The EnMAP satellite has emerged as one of the main hyperspectral resources since its launch in 2022, and has been extensively utilized in various applications, including LULC mapping (Lekka et al., 2024) and methane mapping (Roger et al., 2024) by the scientific community across diverse disciplines, such as soil, forests, agriculture, urban, natural hazards, geology, and more (Storch et al., 2023). Hyperspectral sensors that capture data across numerous narrow, adjacent bands have electromagnetic spectra spanning wavelengths that

* Corresponding author.
E-mail address: abriha.david@science.unideb.hu (D. Abriha).

https://doi.org/10.1016/j.gr.2025.03.014
Received 2 April 2024; Received in revised form 23 March 2025; Accepted 24 March 2025
Available online 20 April 2025

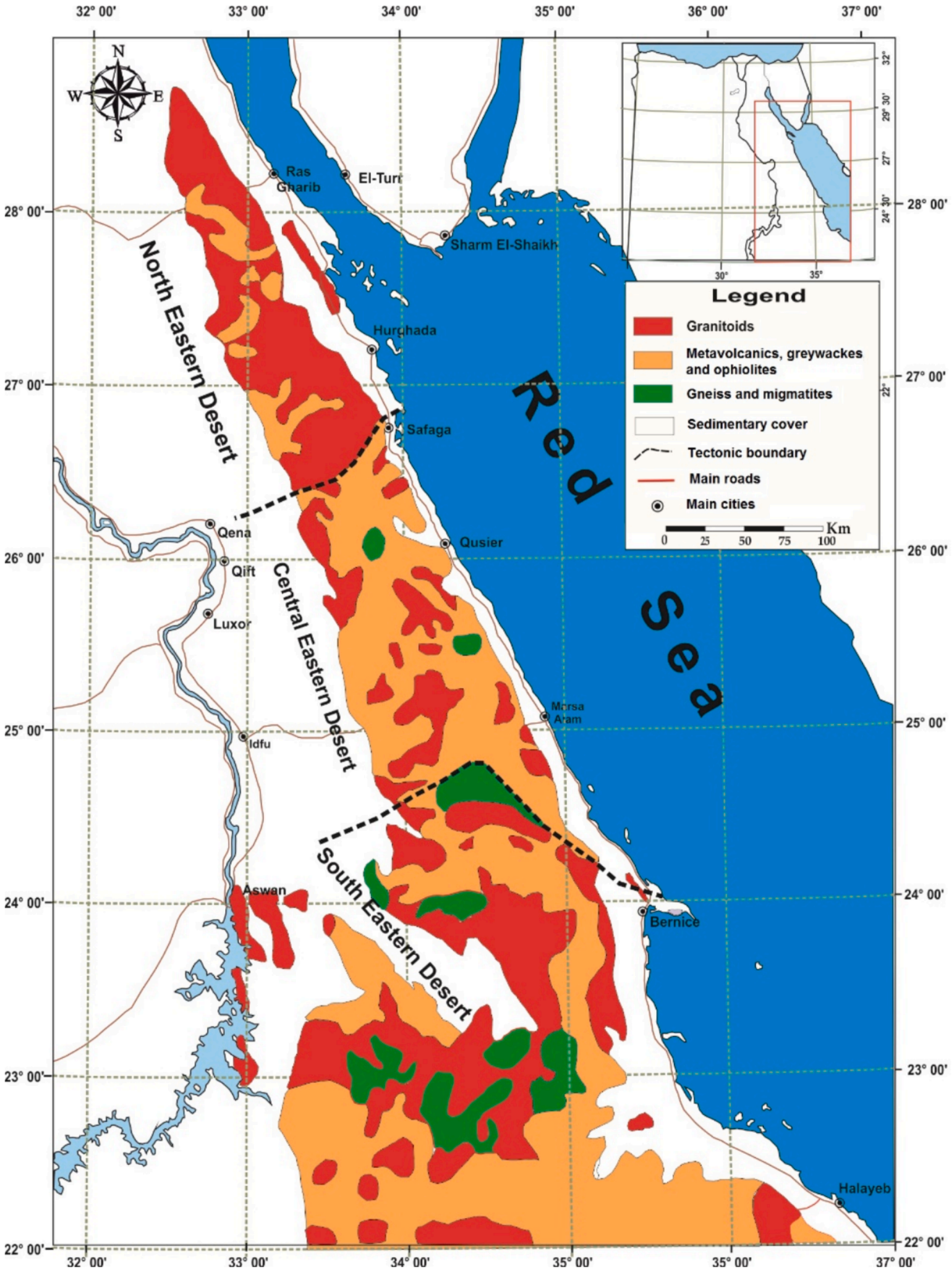

Fig. 1. The threefold structural domains of the Eastern Desert, Egypt.

encompass the visible/near-infrared (VNIR; 350–1000 nm), shortwave infrared (SWIR; 1000–2500 nm), mid-wave infrared (MWIR; 3000–5000 nm), and longwave infrared (LWIR; 8000–12,000 nm) wavelengths (Douglas et al., 2022; Goetz et al., 1985; Shebl et al., 2023b). A crucial attribute driving the endorsement of hyperspectral sensor data is its capacity to discern complicated surface materials with precision (Bioucas-Dias et al., 2013; Shebl et al., 2023b; Singh et al., 2020). The composition and surface roughness of materials can be determined by analyzing the wavelengths at which incoming photons are reflected. This process enables the identification of specific minerals

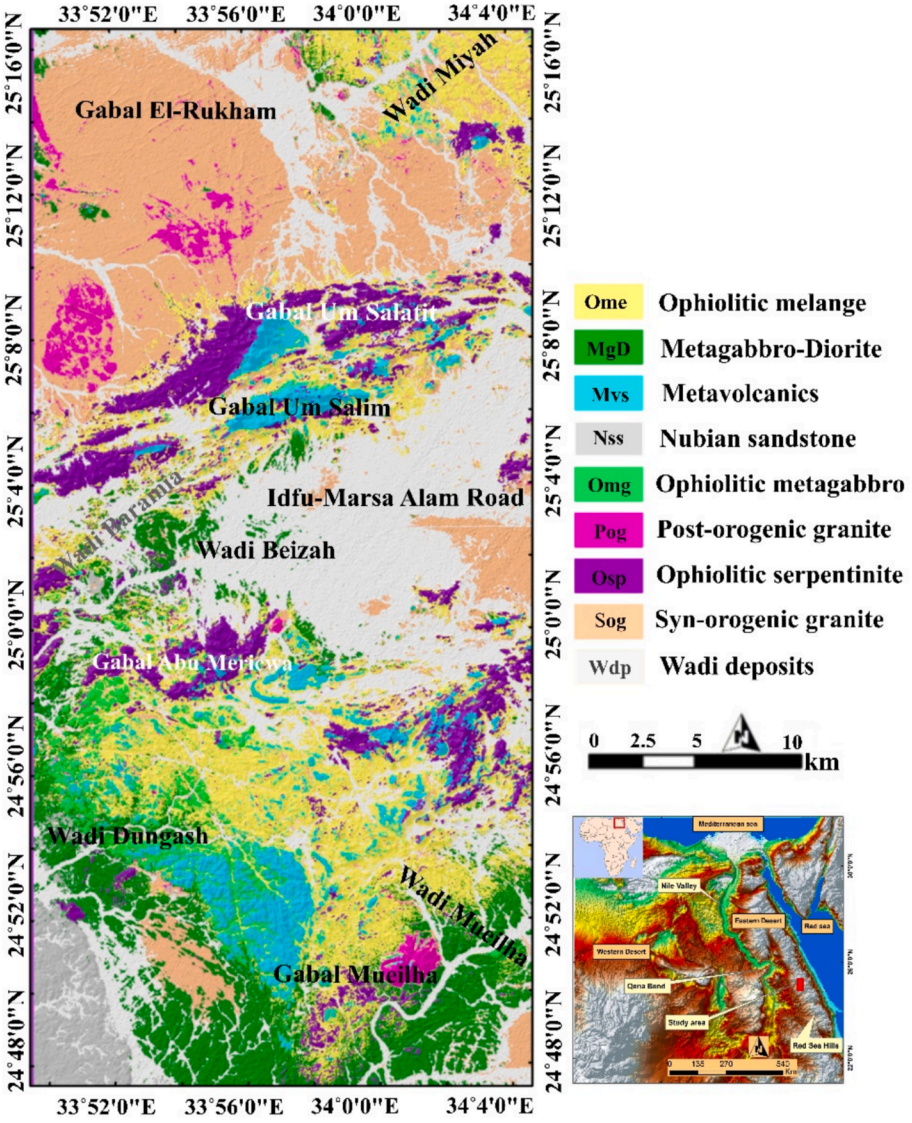

Fig. 2. Lithological map of the study area modified after (Shebl and Csámer, 2021).

and mineral groups by examining their unique absorption features (Savitri et al., 2021; Simpson and Rae, 2018).

On April 1, 2022, a SpaceX Falcon 9 rocket from the Cape Canaveral, Florida, was used to launch the EnMAP satellite. It is intended to continue functioning for five years. One of the primary objectives of EnMAP is to foster natural resource management, encompassing geological considerations, such as mineral deposits and groundwater sources (https://www.enmap.org/science/). Additionally, it is expected to provide a more accurate delineation of the industrial impacts, including mining activities, on natural resources. From a geological perspective, a plethora of remote sensing data, spanning from panchromatic to multispectral and imaging spectroscopy, have proven capable of facilitating comprehensive lithological and hydrothermal alteration mapping (Adiri et al., 2020; Badawi et al., 2022; Bedini and Chen, 2022; Sabins, 1999; Shebl et al., 2021a). The effectiveness of these tasks mainly relies on the sensor used and the types of rocks present in the study area. For example, it's often easy to distinguish between metamorphic rocks with clear foliation, sedimentary rocks with distinct bedding patterns, and igneous rocks with their massive shapes without needing detailed spectral data. However, spectral information is crucial when differentiating between rocks in the same geological category. For instance, distinguishing between acidic and basic igneous rocks is possible using appropriate RGB spectral combinations.

In addition to spectral information obtained from remote sensing data, airborne geophysical measurements, particularly aeromagnetic and Aeroradiometric surveys, have played a significant role in identifying areas of hydrothermal alteration as well as in describing and distinguishing between various rock units based on their magnetic intensity variations or radioelement signatures (Amigun et al., 2022; Elkhateeb and Abdellatif, 2018; Harris et al., 2009; Sanusi and Amigun, 2020a, Sanusi and Amigun, 2020b). Several enhancement techniques have been developed for these targets (Duval, 1983; Nabighian, 1974; Ostrovskiy, 1975). This success increased with the integration of these data (Abdelkader et al., 2024; Afolabi et al., 2024; Sanusi et al., 2024a; Sanusi et al., 2024b;Sanusi and Amigun, 2020a, Sanusi and Amigun, 2020b) with remote sensing data from each other, and together, they achieved a major breakthrough in indirect research on mineralized areas by identifying criteria that indicate the presence of important ore deposits (Colin V. Reeves, 1990; Shebl et al., 2023a, 2021b).

As the complexity of geological targets increases, the demand for a rich array of spectral data intensifies, highlighting the indispensability of imaging spectroscopy. Consequently, this study applied EnMap data to discern various geological formations, including ophiolitic mélange rocks, island arc metavolcanics, metagabbroic formations, granitic structures, quaternary deposits, and mining activities within the Egyptian Eastern Desert. This study addresses the research gap concerning

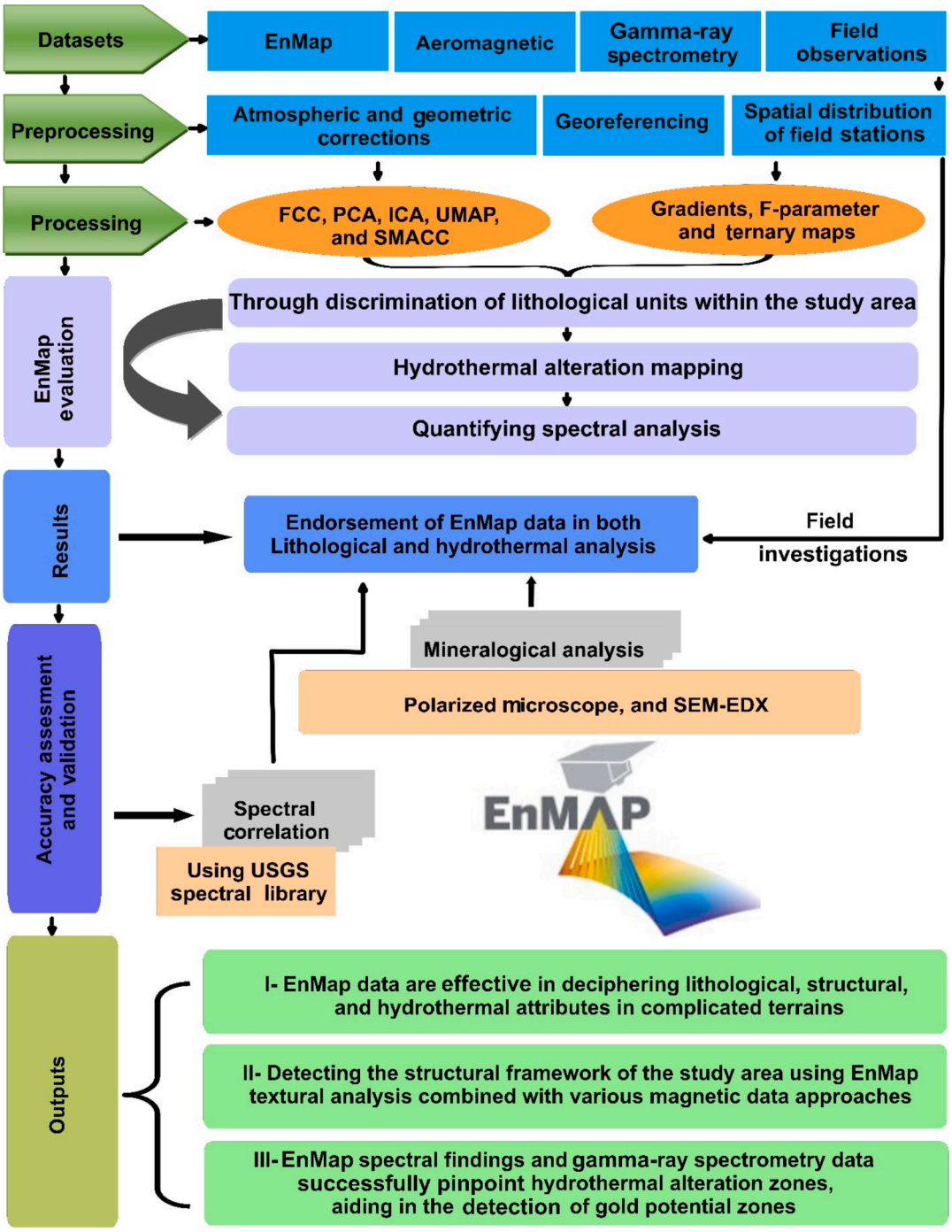

Fig. 3. Methodological flowchart outlining the applied methods and the datasets utilized in the study.

the underexplored potential of EnMAP hyperspectral data, which, as a new free and globally available resource, is expected to see extensive use in the near future. We evaluate EnMAP's effectiveness for detailed geological mapping and mineral exploration in arid regions like the Arabian Nubian Shield (ANS), focusing on its capabilities in identifying lithologies, geological structures, hydrothermal alterations, and gold mineralization zones, with validation through geophysical and field data integration. Furthermore, this study provides updated insights into the lithological, structural, and hydrothermal alteration characteristics of the study area using EnMap data.

2. Study area and geological setting

The juvenile Neoproterozoic Arabian-Nubian Shield (ANS) constitutes the north-eastern segment of a regional collision zone between East and West Gondwana, known as the East African Orogen (EAO) (Abd El-Wahed and Attia, 2023, Abd El-Wahed and Attia, 2022; Greiling et al., 1994; Hamimi and Abd El-Wahed, 2020; Johnson and Woldehaimanot, 2003; Stern et al., 2004). The evolution of ANS included three stages: (a) an intra-oceanic subduction and subsequent arc accretion; (b) a stage of orogenic extension; and (c) a post-extensional compressional stage (Abd El-Wahed and Hamimi, 2021; Hamimi et al., 2021; Johnson and Woldehaimanot, 2003).Various endogenous mineralization are related to

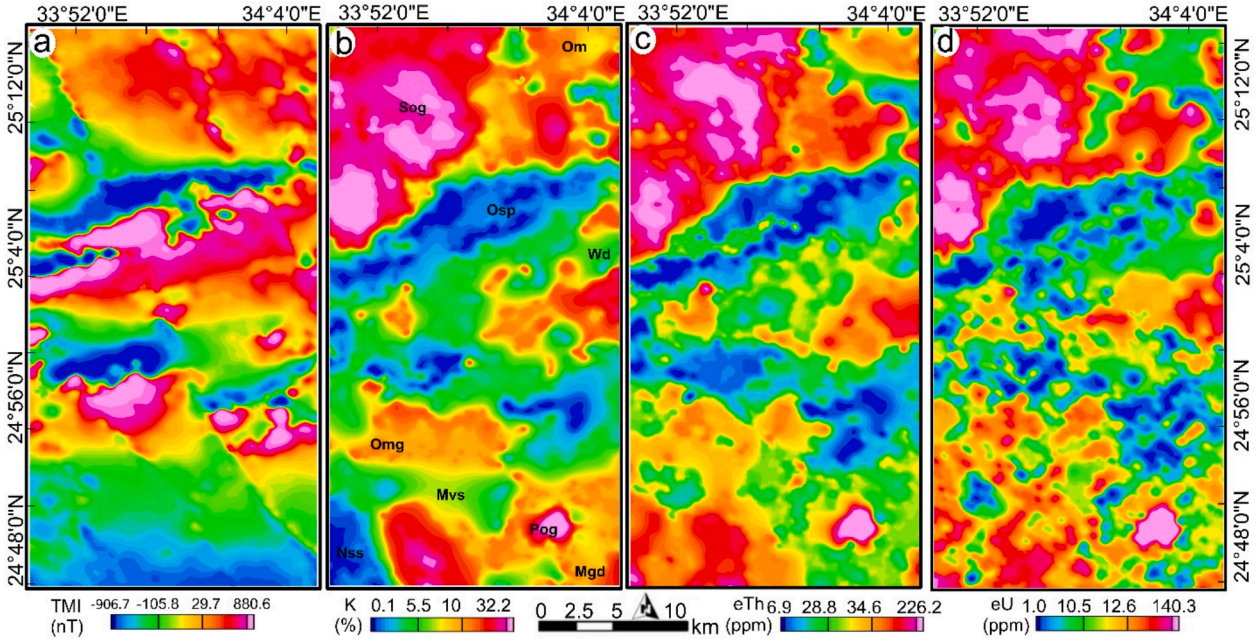

Fig. 4. Airborne geophysical data: a) Total magnetic intensity map after removing geomagnetic effect, b) Potassium concentration, c) Equivalent thorium concentration, d) Equivalent uranium concentration. Ophiolitic serpentinite (Osp), volcaniclastic metasediments as an ophiolitic mélange matrix (Ome), metavolcanics (Mvs), metagabbro-diorite (MgD), *syn*-orogenic granite (Sog), post-orogenic granite represented by mueilha granite (Pog), nubian sandstone (Nss), and wadi deposits (Wdp).

each stage of ANS evolution. According to (Ahmed, 2022), these mineral deposits can be categorized into four distinct types: (1) Magmatic mineral deposits linked to mafic–ultramafic rocks, which include chromite, Ni-Cu-Co-PGE magmatic sulfides, and Fe-Ti-V oxides. (2) Intrusion-related deposits of a magmatic-hydrothermal nature associated with felsic to intermediate rocks, such as porphyry, epithermal Au-Ag/sulfide vein types, skarn, and granite-related pegmatite-REE deposits. (3) Hydrothermal orogenic gold deposits and volcanogenic massive sulfide (VMS) deposits. (4) Surficial mineral deposits, which encompass chemical-sedimentary, residual, mechanical, and supergene enrichment deposits.

The study area is located in the extreme southern part of the central Eastern Desert along its boundary with the southern Eastern Desert, which is known as the Sha'it-Nugrus shear zone (Fig. 1). This ~ 200 km-striking, northerly dipping, low-angle, normal ductile shear zone formed in a post-arc collision extensional tectonic setting about 600 Ma (Abd El-Wahed et al., 2019; Abd El-Wahed and Attia, 2022; El-Ramly, 1984; Fowler and El Kalioubi, 2002; Fowler and Osman, 2009; Hamimi et al., 2018; Mostafa et al., 2022). Strong deformation and metamorphism along the shear zone affected most lithologies in the area, which encompass high-grade gneisses (e.g., Migif-Hafafit), metavolcanics, metasediments, granitic gneisses, and ophiolitic mélanges and contributed to the formation of various orogenic gold mineralizations, including Hangaliya, El-Baramiya, and Hamash. Gold mineralization can be related to major subsequent three deformation phases recorded by Hamimi et al. (2018), including: (a) NE-SW shortening Dl phase, (b) transpressional D2 phase, and NE-trending dextral shearing phase D3.

The predominant ophiolitic mélange, low-grade metavolcanic rocks with their related mafic–ultramafic intrusions in the central (CED) and southern Eastern Desert (SED), host significant related ore deposits, particularly podiform chromite deposits found in the Gerf and Abu Dahr areas, which manifest as extensive, continuous masses. These chromite deposits are occasionally associated with platinum group metals, as noted by Styles et al. (1996). Additionally, several areas, including Abu Ghalaga, Umm Effein, Umm Ginud, Kolmnab, Wadi Rahaba, Abu Dahr, Hamra Dome, and Wadi El-Miyah, host titaniferous iron ores (Amin, 1954; Basta and Takla, 1968; El-Shazly, 1959). The volcanic rocks found in the Um Samiuki and Darhieb deposits represent some of the largest volcanic massive sulfide deposits in Egypt. Furthermore, the CED and SED also host various orogenic gold mineralizations associated mainly with greenstone belts, as identified by (Zoheir and Weihed, 2014). The highest concentration of gold deposits in the Eastern Desert is linked to the NW-trending Najd Fault System, which includes numerous shear zones across the major blocks, including the Heiani-Ogadeer shear zone and the Duwag shear zone. According to (El Kazzaz, 2012) and (Zoheir et al., 2019), the shearing events were triggered by the collision of eastern and western Gondwana during the late Cryogenian to Ediacaran period (640–542 Ma). Likewise, the occurrence of gold mineralization in the East Barramiya area is related to this post-accretionary stage recognized throughout the Eastern Desert (Zoheir and Lehmann, 2011).

The East Barramiya area is situated within the Egyptian basement rocks, a constituent of the broader ANS. According to (Abdelsalam and Stern, 1996; Stern, 1994), the ANS is recognized as the northern extension of the Mozambique belt, representing an example of accretionary orogens and suturing. Comprising primarily ophiolitic components and an island arc assemblage, the Egyptian basement rocks also feature significant intrusion of massive granitic formations (Shackleton, 1988). Similar to the regional geology of the Egyptian basement rocks, the study area consists of imbricated layers of ophiolitic rocks intermingled with volcanic and sedimentary rocks from an island arc assemblage (Fig. 2). The area exhibits granitoid and gabbroid intrusions (Shebl et al., 2022; Zoheir et al., 2019). These intrusions have penetrated the pre-existing rocks, occasionally altering the primary structures (Shebl and Csámer, 2021a). The study area's southwestern region is overlaid by Phanerozoic Nubian sandstone, spanning from the Cambrian to the Upper Cretaceous period. The study area lies eastward of the Gabal Barramiya serpentinite and encompasses an extensive region stretching from Gabal El-Rukham in the north to Gabal Um Salatit and Dungash, to Gabal Mueilha in the south.

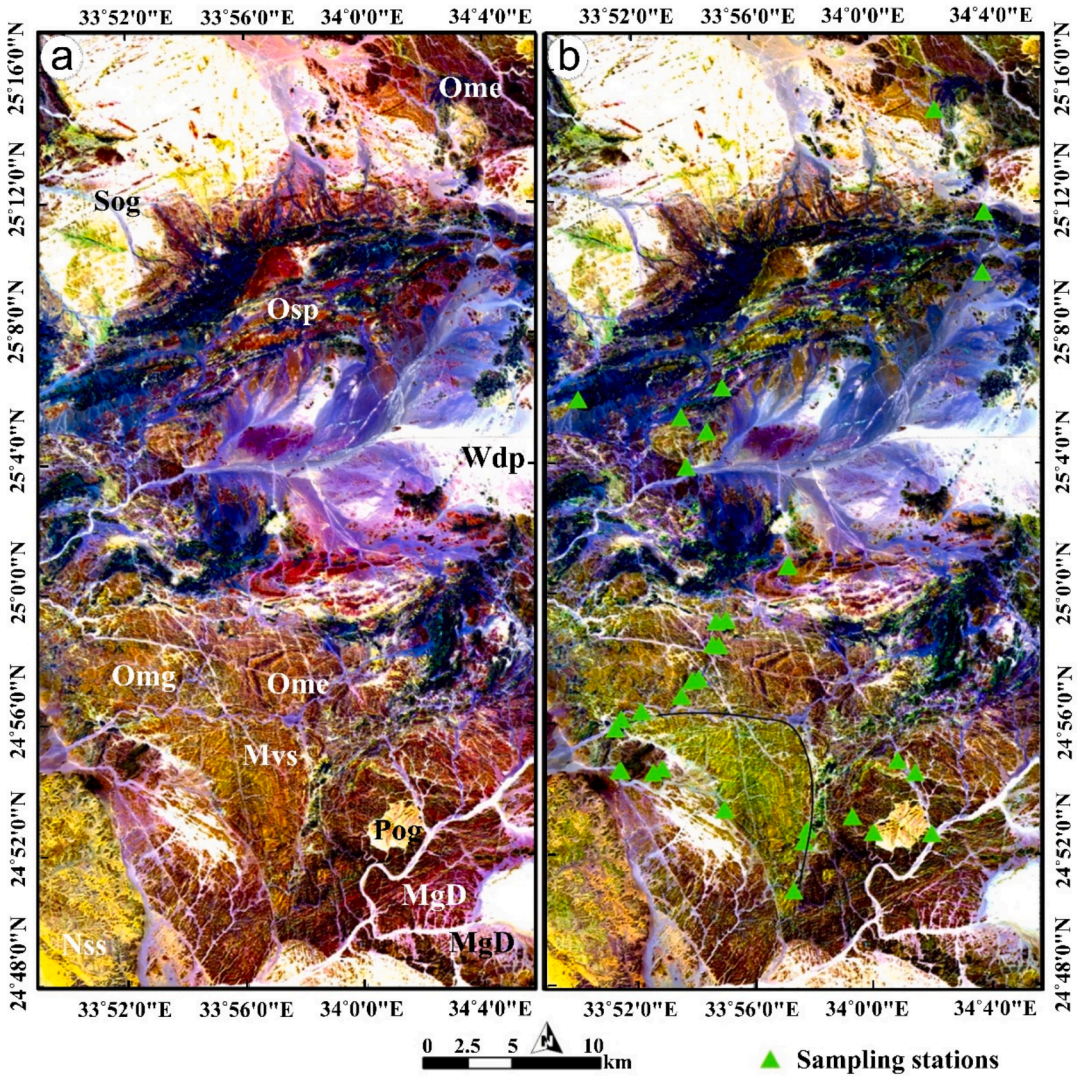

Fig. 5. EnMap FCCs using wavelengths (nm) of a) 2445.30 (b224)-1187.20 (b118)-429.45 (b3) and b) 2445.30 (b224)-1553.01 (b145)-477.74 (b13) in RGB, respectively, discriminating the main rock units in the study area. Ophiolitic serpentinite (Osp), volcaniclastic metasediments as an ophiolitic mélange matrix (Ome), metavolcanics (Mvs), metagabbro-diorite (MgD), *syn*-orogenic granite (Sog), post-orogenic granite represented by mueilha granite (Pog), nubian sandstone (Nss), and wadi deposits (Wdp).

3. Materials and methods

3.1. EnMap hyperspectral data

A push-broom-style hyperspectral imager on board the EnMAP satellite captures reflected solar radiation from the Earth's surface in 246 consecutive bands between 420 and 2450 nm. In the VNIR range, the mean bandwidth is 6.5 nm, while in the SWIR range, it is 10 nm. The sensor has a spatial resolution of 30 m and offers a swath width of 30 km. With a daily capability of 5000 km, EnMAP has the capability to capture strip lengths ranging from 30 km to 1000 km. While the nominal target revisit time is set at 27 days, this can be significantly reduced to just 4 days through the use of an across-track off-nadir pointing capability of ± 30°. EnMAP operates within a sun-synchronous orbit positioned at an altitude of 653 km with an inclination of 97.96°, ensuring a local equatorial crossing time of 11:00 ± 00:18 hr(Storch et al., 2023).

A signal-to-noise ratio (SNR) of ≥ 400:1 in the VNIR and ≥ 170:1 in the SWIR, alongside a radiometric calibration accuracy exceeding 5 % and a spectral calibration uncertainty of 0.5 nm in both VNIR and SWIR, ensures precise radiometric and spectral responses. The present study utilized two scenes of EnMAP Level 2A data (geo-referenced bottom-of-atmosphere reflectance), which is derived from processing the Level 1C product (top-of-atmosphere radiance) through a Level 2A processor (Bachmann et al., 2021). The data was accessible through the Scientific Category-1 User role, which is granted high-priority status following technical evaluation and approval of the submitted research proposal. A comprehensive flowchart illustrating the methodology, including the datasets utilized and the methods applied, is presented in Fig. 3.

3.2. Airborne geophysical data

The inspected area is encompassed in the airborne geophysical survey completed by the Aero-Service division of Western Geophysical Company of America (Aero-Service, 1984), which covers a large section of the northern, central, and southern Red Sea Mountains in the eastern desert of Egypt. This survey is considered a joint Egyptian American undertaking, of the assessment program for groundwater, petroleum, and minerals. The survey was Following parallel flight lines oriented in a NE-SW direction at 1 km spacing with an azimuth of 45° and 225° from the true north. meanwhile, the tie lines were flown in a NW-SE direction at right angles to the main flight line direction with an azimuth of 135° and 315° from the true north. The flight altitude was 120 m terrain

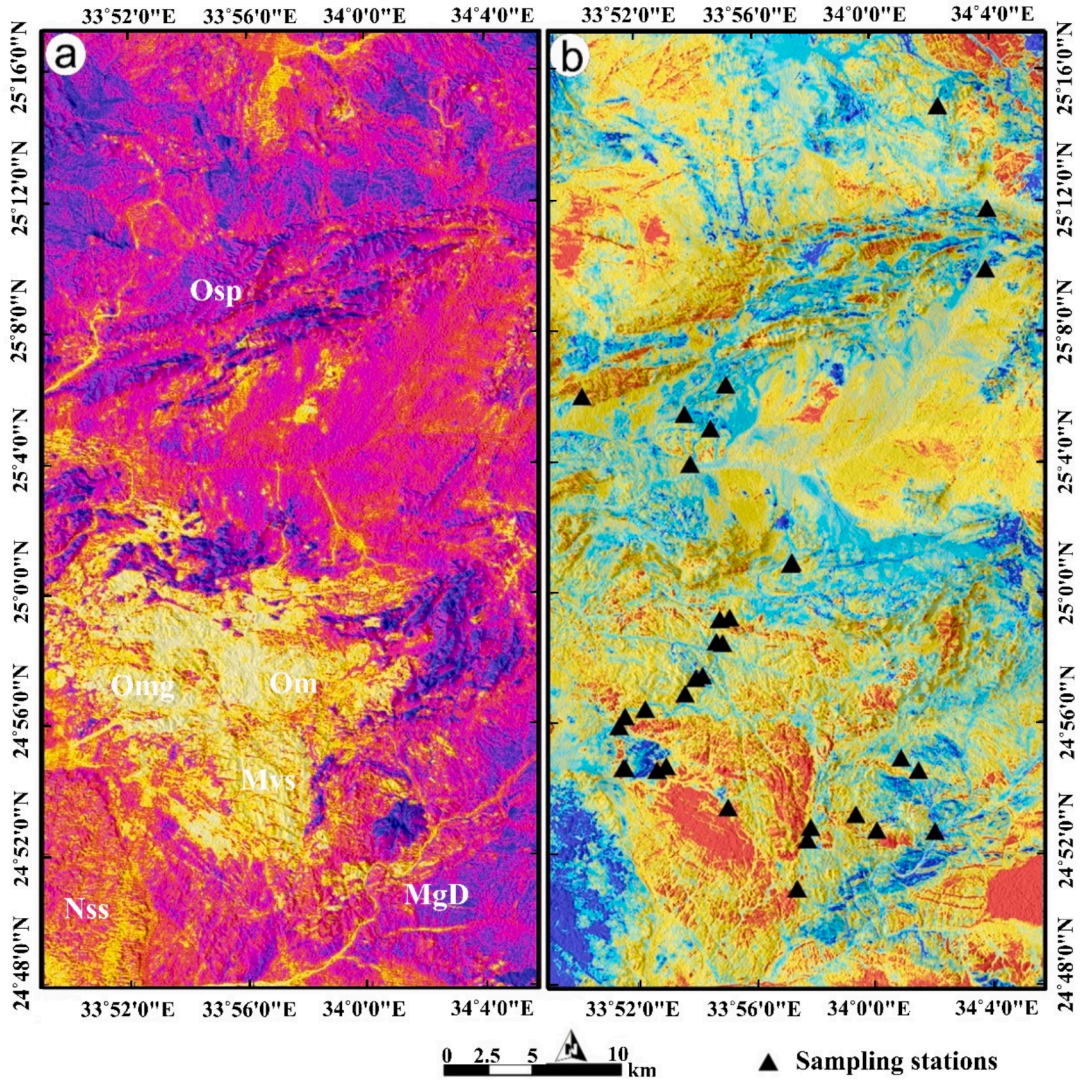

Fig. 6. Pseudocolor ramps of a)PC 10 discriminating island arc metavolcanics and volcaniclastic metasediments (yellow) and b) PC6 highlighting acidic rocks (red) within the study area. (For interpretation of the references to color in this figure legend, the reader is referred to the web version of this article.)

clearance, and the inclination and declination of the magnetic field were 32.8 north and 1.9 east respectively. Diurnal variations effects on the magnetic field were reduced. Also, international geomagnetic reference field (IGRF) was declined from the total magnetic intensity measurements to get rid of the regional gradient of the earth's magnetic field because of the frequent changes in the magnitude and direction of earth's magnetic field from one place to another (Dobrin, 1976). The aeromagnetic and spectral gamma-ray measurements were pre-processed, corrected (e.g., calibration, atmospheric correction, georeferencing), complied, and illustrated in the form of contour maps. The available contour maps are total magnetic intensity anomaly (TMI), Potassium (k), Equivalent thorium (eTh) and Equivalent uranium (eU) concentrations are digitized in numeric format that allows the application of interpolation (gridding) techniques and then displayed in colored maps (Fig. 4) for further processing.

3.3. Methods

3.3.1. Image processing techniques

After conducting thorough band animation and drawing on previous research, it is evident that while False Color Composite (FCC) remains a conventional technique, it offers crucial spectral information that enables discrimination among exposed rock units through straightforward RGB combinations (Shereif et al., 2024). The combinations employed included bands from both the VNIR and SWIR ranges (e.g., bands b224-b118-b3 in RGB and b224-b145-b13 in RGB).

Principal component analysis (PCA) was utilized to scrutinize EnMap data for lithological discrimination. Typically, PCA serves as a significant tool for reducing the dimensionality of hyperspectral data. PCA is considered a type of unsupervised classification as it extracts a concise set of features that encapsulate the essence of the data, such as an optimized spectrum of wavelengths(Abd El-Wahed and Hamimi, 2021; Balázs et al., 2018; Khedr et al., 2023). Principal components (PCs) are linearly uncorrelated variables produced through an orthogonal transformation from a dataset by principal component analysis (PCA). The sequence of these converted PCs is such that the first one represents the maximum variability in the data, and the remaining variance is contained in each successive component in descending order (Abdelkader et al., 2022). In this study, PCA was applied to the entire EnMap bands to visually discriminate the rock units at a pixelated level. Independent component analysis (ICA), as a widely recognized technique for separating sources without prior knowledge, is applied to EnMap data. This method decomposes a given set of mixed signals into a collection of sources or components that are statistically independent (ICs) (Kumar et al., 2020; Shebl et al., 2021b).

Besides PCA and ICA, a recently proposed dimensionality reduction

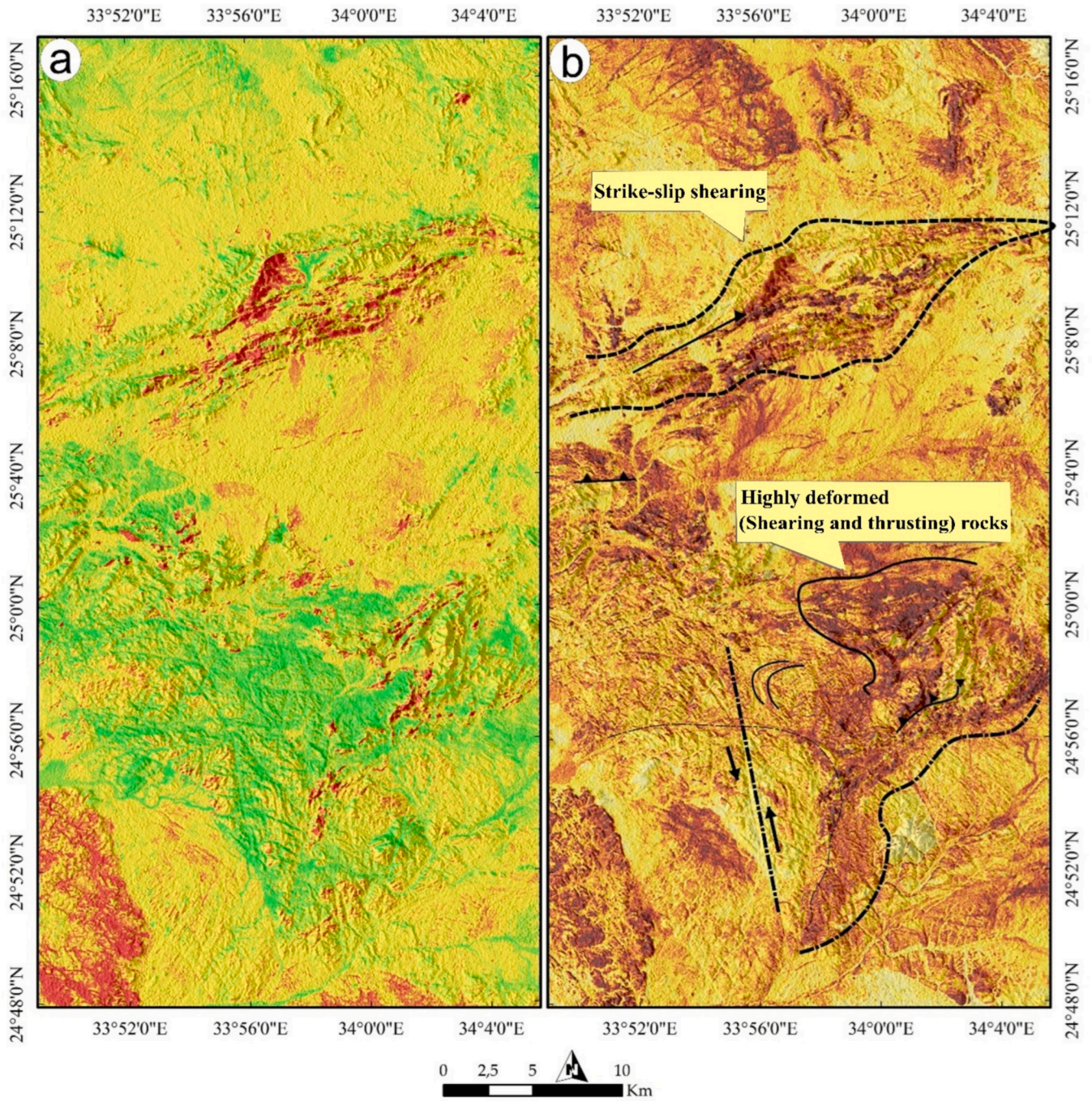

Fig. 7. Pseudocolor ramps of a) PC11 showing mainly talc carbonates in red and their link to b) highly deformed zones shown in dark brown through PC14. (For interpretation of the references to color in this figure legend, the reader is referred to the web version of this article.)

method (UMAP) was applied to check the separability of our lithological targets. Uniform Manifold Approximation and Projection (UMAP), a novel manifold learning algorithm (proposed in 2018 by McInnes et al.) designed for dimension reduction, drawing on principles from topological data analysis (McInnes et al., 2018). UMAP is a nonlinear dimension reduction algorithm. At its core, UMAP is utilized to transform the high-dimensional feature representation into a lower-dimensional Euclidean space. As a nonlinear dimension reduction technique, UMAP is rooted in manifold learning principles. It operates on the supposition that high-dimensional data exhibit uniform distribution across local manifolds, thereby constructing a topological depiction of the dataset (Schmitz et al., 2021). This technique has found application across various studies (Myasnikov, 2020; Schmitz et al., 2021), endorsing UMAP's capabilities in maintaining overall data structure, computational efficiency, and effective handling of large datasets. However, in the current research, PCA, a well-known conventional dimensionality reduction technique, yielded reasonable separation of the studied rock units. We anticipated a better representation of our lithological targets by applying the UMAP algorithm to EnMap data lithological features. Reference data for eight lithological targets, including serpentinites (1), basic metavolcanics (2), talc carbonates (3), acidic metavolcanics (4), post-orogenic granite (5), metagabbro-diorite (6), *syn*-orogenic granite (7), and wadi deposits (8), were delineated and used for separability analysis using the UMAP implementation provided by PyPI.

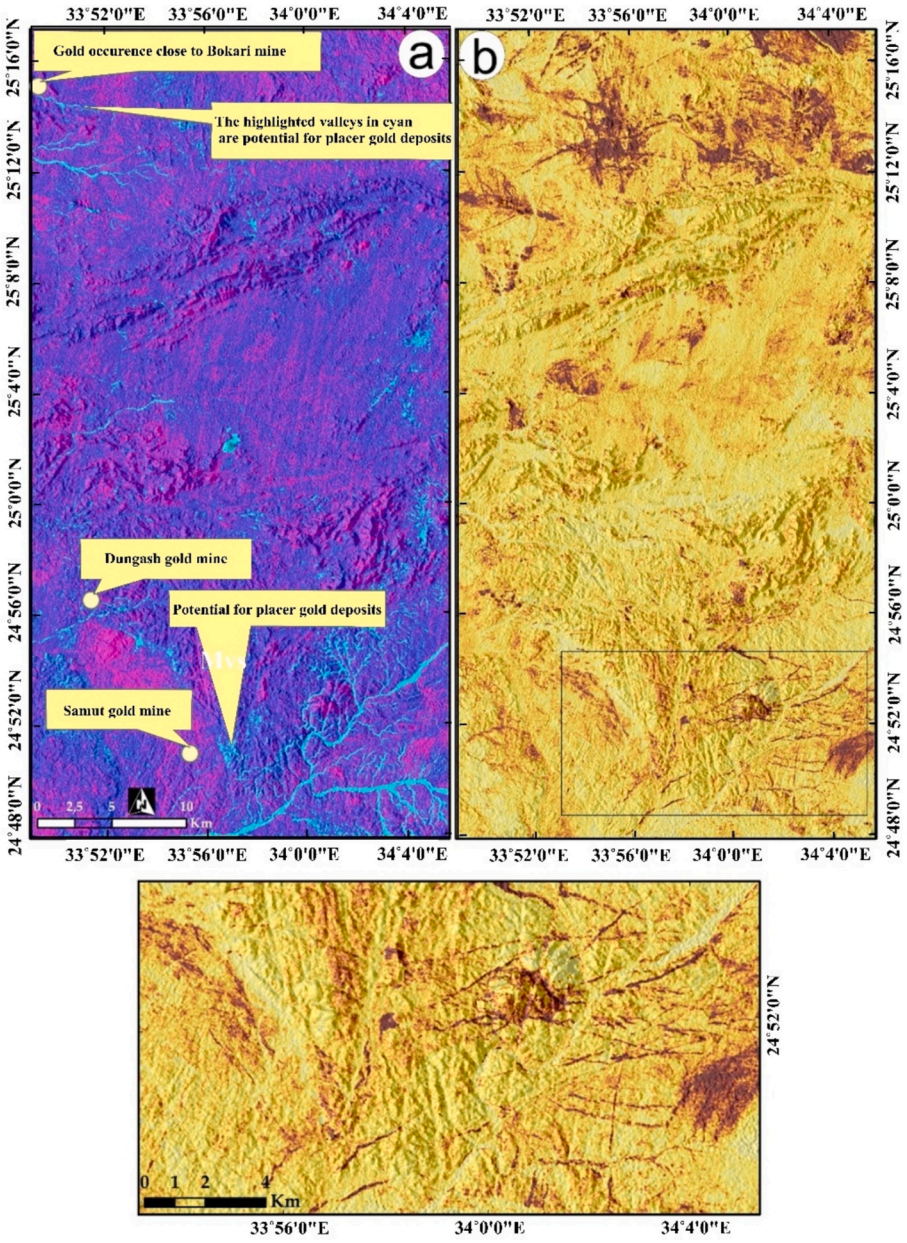

Fig. 8. Pseudocolor images of a) IC22 highlighting primary drainage tributaries and their associated placer deposits (cyan), and b) IC14 demonstrating the structural control on drainage patterns (enlarged map details the southern region for clarification). (For interpretation of the references to color in this figure legend, the reader is referred to the web version of this article.)

3.3.2. Sequential maximum angle convex cone (SMACC)

SMACC is a rapid, completely automated algorithm for identifying endmembers and unmixing, utilized mostly with hyperspectral data where significant correlation among channels and pixels can hinder the effectiveness of unmixing using conventional techniques(Aggarwal and Garg, 2015; Devi and Kalaivani, 2023). As the name suggests, vector data is represented using a convex cone model. The dataset is used to directly pick endmembers using the algorithm. The convex cone model starts with a single endmember and progressively increases in dimension to find these endmembers. At every stage, abundance maps are continuously generated and modified. The angle of a new endmember concerning the current cone is used to identify it. The next endmember to be added to the endmember set is the data vector that has the largest angle in relation to the current cone. The algorithm makes sure that both the current and prior endmember abundances stay positive or zero by updating the abundances of the endmembers that came before them. When every data vector, within a given tolerance, falls inside the convex cone, the process is finished (Aggarwal and Garg, 2015).

Spectral correlation analysis utilized EnMap spectral curves to identify rock types (mineral associations) or specific minerals by analyzing their distinct absorption signatures, referencing spectral curves from well-known libraries such as USGS. The accuracy of these identifications depends on the precise location and strength of absorption features at specific wavelengths within the VNIR-SWIR spectrum.

3.3.3. Aeromagnetic and Aeroradiometric enhancement methods

Principally, the present work considered the analysis and interpretation of Aeromagnetic data (TMI map) and Aeroradiometric data (k, eTh, and eU) to map the structural features, hydrothermal alteration zones and different lithological units deduced by EnMap data. The following approaches are involved in achieving our purposes,

i) Gradient techniques.

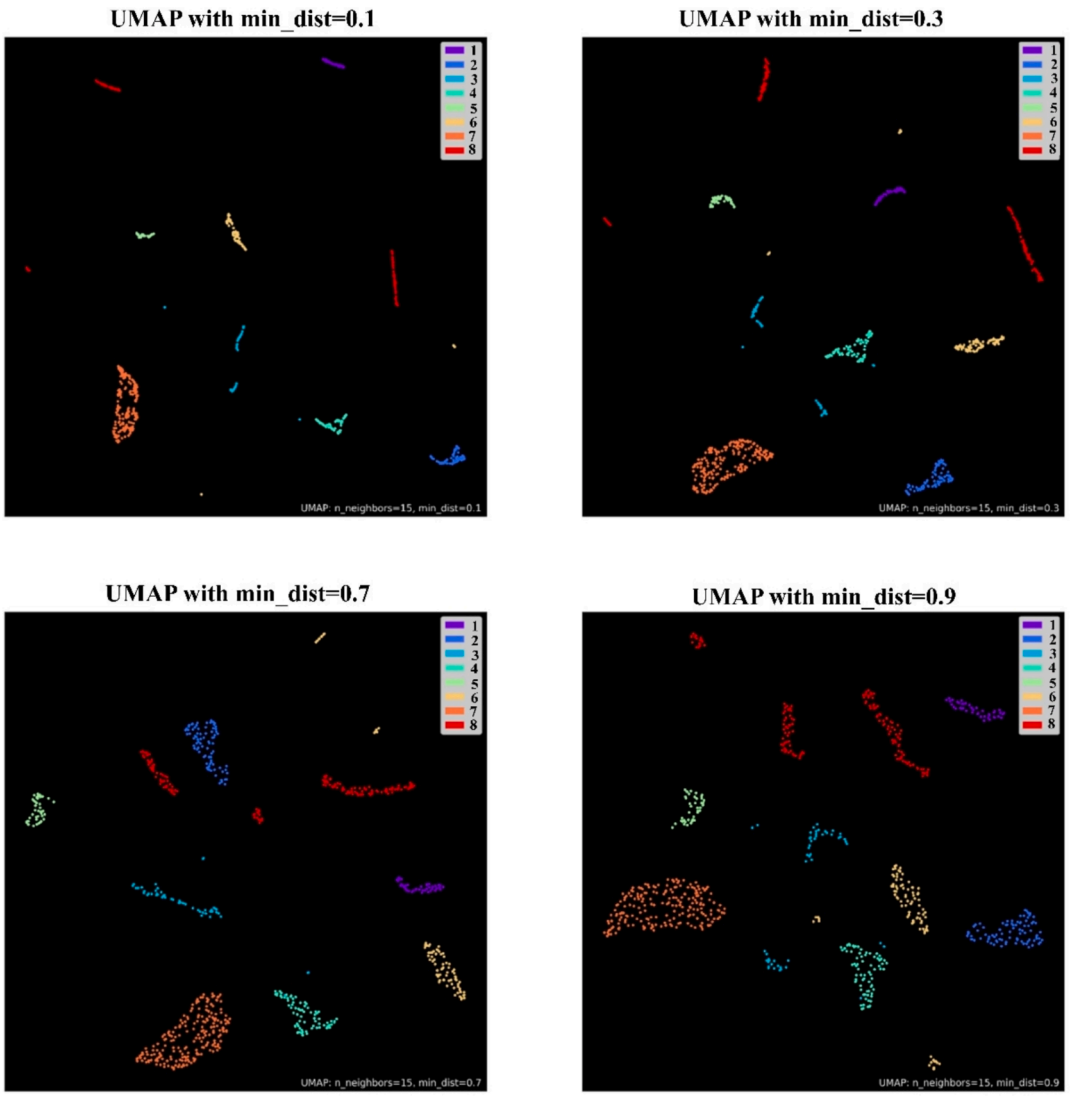

Fig. 9. Examining 2D feature embeddings generated from various distances using UMAP. Serpentinites (1), basic metavolcanics (2), talc carbonates (3), acidic metavolcanics (4), post-orogenic granite (5), metagabbro-diorite (6), *syn*-orogenic granite (7), and wadi deposits (8).

Gradient or in another word derivative techniques have shown a significant role in analysis of aeromagnetic data for delineating structural features related to mineralization. Consequently, in our study we used a set of filters based on the derivative functions such as horizontal derivative in x and y directions (Cordell and Grauch, 1985), first vertical derivative, horizontal gradient (Blakely and Simpson, 1986) and tilt angle derivative (Miller and Singh, 1994) for precisely delineate structural features (e.g., faults, contacts, dykes) that are controlling mineral occurrences.

ii) Ratio and ternary techniques.

The surface concentrations of radioelements k, eU, and eTh can be estimated by measuring gamma ray radiation intensities, which can then be linked to surface concentrations using proper calibration processes (Darnley et al., 1970). These data are then utilized to create maps that depict the distribution of the three radioelements and their ratios for lithological and hydrothermal alterations purposes. The F parameter suggested by (Efimov, 1978)was conducted to map zones that were hydrothermally altered because of the richness of K and eU related to the eTh/K and eTh/eU ratios respectively. Also, a ternary composite map resulting from modulating concentrations of K, eTh and eU can be distinguished into different lithological units (Duval, 1983).

3.4. Lab studies

From over 100 visited field stations, a total of more than 30 rock samples (Figs. 5 and 6), representing all studied rock units within the area, were analyzed. Petrographic investigations were conducted initially, with thin sections prepared from representative rock samples collected from various rock exposures. These samples were examined using a transmitted polarized light microscope to accurately classify the rock types and identify key mineral assemblages. Subsequently, Scanning Electron Microscopy coupled with Energy Dispersive X-ray Spectroscopy (SEM-EDX) was used to validate the petrographic findings, providing high-resolution imagery and elemental data to confirm the presence of ores and their associated minerals, particularly gold. The rationale for employing these techniques lies in their capacity to corroborate remote sensing data, enhance the geological understanding of the region, and facilitate the direct detection of gold.

These methods were chosen based on their reliability in mineral identification and precision in characterizing fine-scale mineralogical features, essential for confirming remote sensing results. SEM-EDX, in particular, was employed due to its high sensitivity and precise detection limits for gold and associated minerals, thereby providing robust confirmation of mineralization. Petrographic analysis was done through optical microscopy at the University of Debrecen. SEM-EDX was

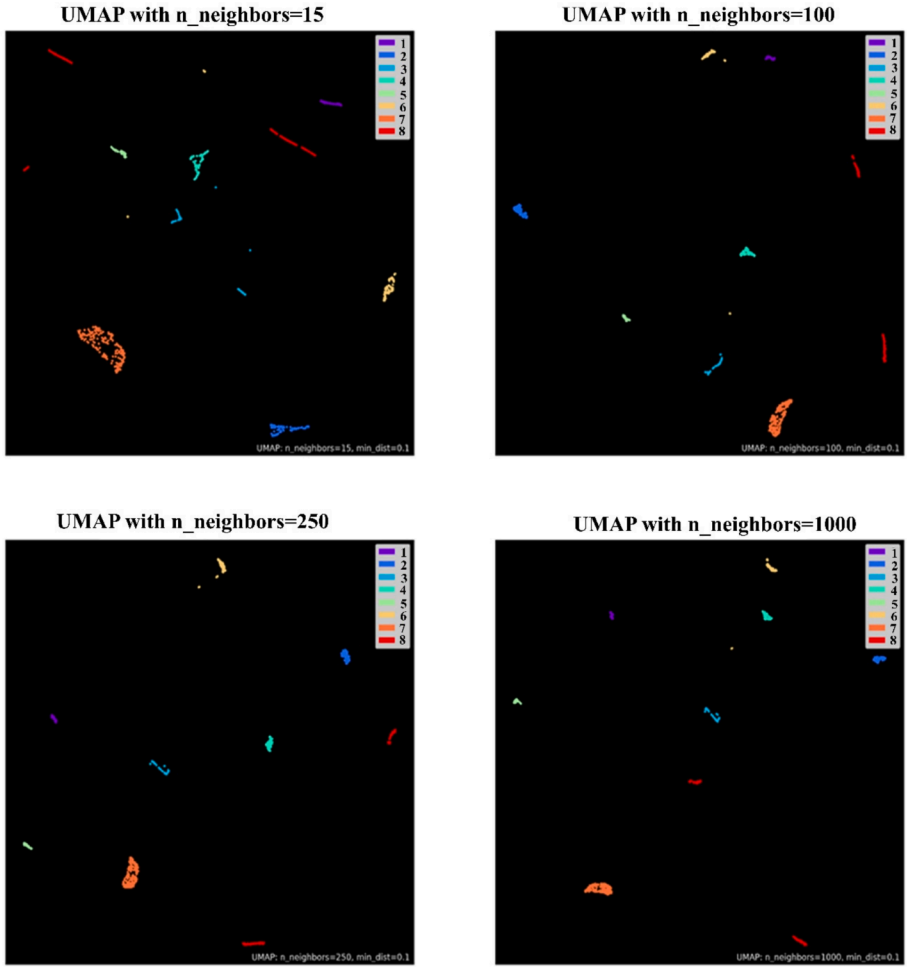

Fig. 10. Examining 2D feature embeddings generated from various numbers of neighbors using UMAP. Serpentinites (1), basic metavolcanics (2), talc carbonates (3), acidic metavolcanics (4), post-orogenic granite (5), metagabbro-diorite (6), *syn*-orogenic granite (7), and wadi deposits (8).

conducted at the Institute of Mineralogy and Geology, University of Miskolc. A SamX-controlled JEOL JXA 8600 Superprobe electron beam microprobe (utilizing a 15–20 kV accelerator voltage and 20nA sample current) was employed, complemented by an SDD-EDX detector.

4. Results and Discussion

4.1. Lithological mapping

Utilizing EnMap data, we differentiated between several lithological units within the study area. Discernible spectral signatures for different materials denote the unique absorption and reflection characteristics across the electromagnetic spectrum. The uniqueness of these signatures stems from the molecular structure and chemical bonds within each substance. For example, the false color composites (FCCs) of bands b224-b118-b3 and b224-b145-b13 in RGB effectively distinguished the exposed lithologies within the study area (Fig. 5). These combinations of VNIR and SWIR wavelengths are particularly capable of discriminating complex basement rocks in such arid terrains (Shebl and Csámer, 2021b).

The FCC of b224-b118-b3 (in RGB, respectively) highlights serpentinite rocks in a dark black color, clearly distinguished from granitic rocks (bright beige to white) and island arc associations (dark red to yellow). Further discrimination was achieved through b224-b145-b13 in RGB respectively, where island arc metavolcanics appeared in a greenish-yellow hue, with a prominent exposure in the southwestern part forming a fold-like structure trending NE-SW (Fig. 5). Metagabbroic rocks appeared in a brown-dark red color to the south of this exposure, while to the north, a complex ophiolitic mélange matrix was represented by mixed brown-yellow colors, indicating their chaotic composition as volcaniclastic metasediments. The study area exhibits a significant level of complexity among its exposed rock units, prompting our current research to resolve this intricacy and be considered a rigorous evaluation of EnMap data. By employing image processing techniques including FCC, PCA, and ICA on EnMap data, we have successfully categorized the majority of rock units. Additionally, spectral data analysis has provided a clear differentiation among various lithological features, contributing to a comprehensive understanding of the complexity along lithological boundaries. For example, Fig. 6a illustrates the PC 10 of EnMap data, effectively delineating island arc metavolcanics and volcaniclastic metasediments in the central western part of the study area, distinct from other lithologies. Furthermore, acidic rocks such as acidic metavolcanics and acidic dykes, along with granitic rocks and their weathering products along the wadis, are prominently displayed in red in Fig. 6b using PC6. PC11 highlighted talc carbonates in red (Fig. 7a), spatially associated with serpentinite rocks and dispersed as blocks across the study area.

Notably, talc carbonate occurrence is linked to structural features such as shearing or thrusting. Examination of their distribution with the main structural features (dark brown zones in Fig. 7b) confirms their association with the deformational events that affected the study area. This finding aligns closely with Zoheir et al. (2019) statement that the existence of rocks containing talc, magnesite, listvaenite, and chromite deposits serves as a key indicator of the tectonic boundaries separating

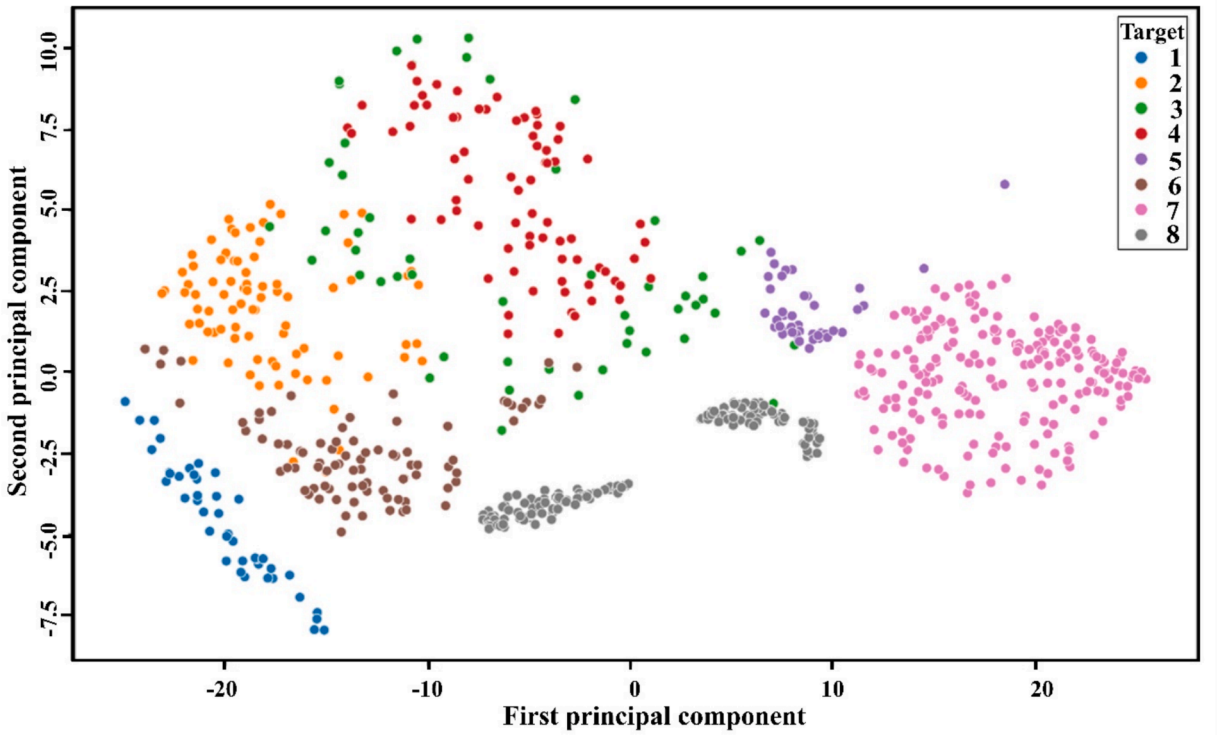

Fig. 11. Visualizing 2D feature embeddings generated using PCA. Serpentinites (1), basic metavolcanics (2), talc carbonates (3), acidic metavolcanics (4), post-orogenic granite (5), metagabbro-diorite (6), *syn*-orogenic granite (7), and wadi deposits (8).

displaced serpentinite masses from the amalgamated matrix of metamorphic sediments. Additionally, analyzing the distribution of talc carbonates (red pixels in Fig. 7a) and identifying the dark brown zones in Fig. 7b, clearly depicts the branching of thrusts in the southern part of the study area, as stated by (Zoheir et al., 2019). In the central portion of the study area, these thrusts are notably linked with ENE-WSW sheared serpentinite blocks. This area is characterized by extensively deformed ophiolite segments, thrust faults predominantly oriented in an ENE–WSW direction, and fewer NW-trending fault lines and shear zones. Within the central zone, ductile shear zones have developed within intensely deformed and folded ophiolitic and island rock formations, hosting various occurrences of orogenic gold within the ophiolitic mélange, exemplified by the Barramiya deposit.

The impact of these deformational events not only influenced the rock units but also played a significant role in shaping the primary drainage patterns (mapped as blue valleys at the southeast corner of Fig. 8a) within the study area. For instance, consistent NE-SW to EW drainage tributaries are evident throughout the study area, as illustrated in Fig. 8a. Furthermore, a trellis drainage configuration is observed in the southeastern part of the study area, situated to the south of Gabal Mueilha. These drainage characteristics are depicted in the IC 22 map (Fig. 8a), where the cyan color distinctly outlines the drainage network while also emphasizing the main placer deposits within the study area.

However, our primary focus in this contribution is to evaluate the lithological and structural controls influencing primary gold deposits within the study area. The EnMap IC22 map, displayed in Fig. 8a, highlights potential placer gold deposits, as indicated by the distribution of cyan pixels. These potential deposits align with the locations of three main gold mines—Bokari, Dungash, and Samut—confirming the map's accuracy in identifying areas with placer gold potential. For instance, in the northern part of the study area, two primary drainage features within the latitudes 25°12′ to 25°16′ N are in close spatial proximity to the Bokari gold mine. In the central region of the study area, and to the south of Gabal Barramiya, the scattered cyan color denotes mining activities within serpentinites and associated rocks, such as talc-carbonates and listvaenites. Around Latitude 24°56′, Wadi Dungash, a NE-SW trending wadi, is notably highlighted as a structurally controlled drainage system, enriched with placer deposits from the Dungash gold mine. To the south of the Dungash gold mine, spots of cyan color indicate placer deposits allocated southwest of the well-known metavolcanic blocks, reflecting the spatial influence of the Samut gold mine. In the southeastern corner of the study area, the structural control of drainage networks is apparent through the trellis drainage pattern, highlighted in cyan, signifying the sporadic mining activities in that region. For a better clarification of the structural control in that area, IC 14 (Fig. 8b) was created, highlighting the cross-cutting relationships and the straightness of the wadis there. Additionally, certain brown areas signify pre-existing structurally controlled mined alteration zones within the study area.

UMAP findings confirmed the lithological discrimination performed by PCA and ICA, with an even emphasis on their spectral separability in 2D representations. We applied UMAP with multiple distances and multiple neighbors to thoroughly investigate the algorithm's results. Maintaining a constant neighbor number of 15, we observed a significant separation among the lithological classes across varied distances (0.1, 0.3, 0.7, and 0.9), as illustrated in Fig. 9. The latter representation showcased our features on different scales (using various distance metrics), providing a more suitable depiction for capturing the underlying structure of the data, particularly its spatial characteristics within each feature (Fig. 10).

Furthermore, another representation demonstrated UMAP's effectiveness in separating these features using a consistent distance of 0.1 with varying neighbor numbers (15, 100, 250, and 1000) in the low-dimensional space. Notably, the optimal separation was achieved with a high number of neighbors, albeit at the cost of increased computational demands and the obscuration of the resulting embedding's characteristics. Regardless of the representation method used, UMAP consistently provides a significantly improved representation of our features compared to PCA when applied to low-dimensional

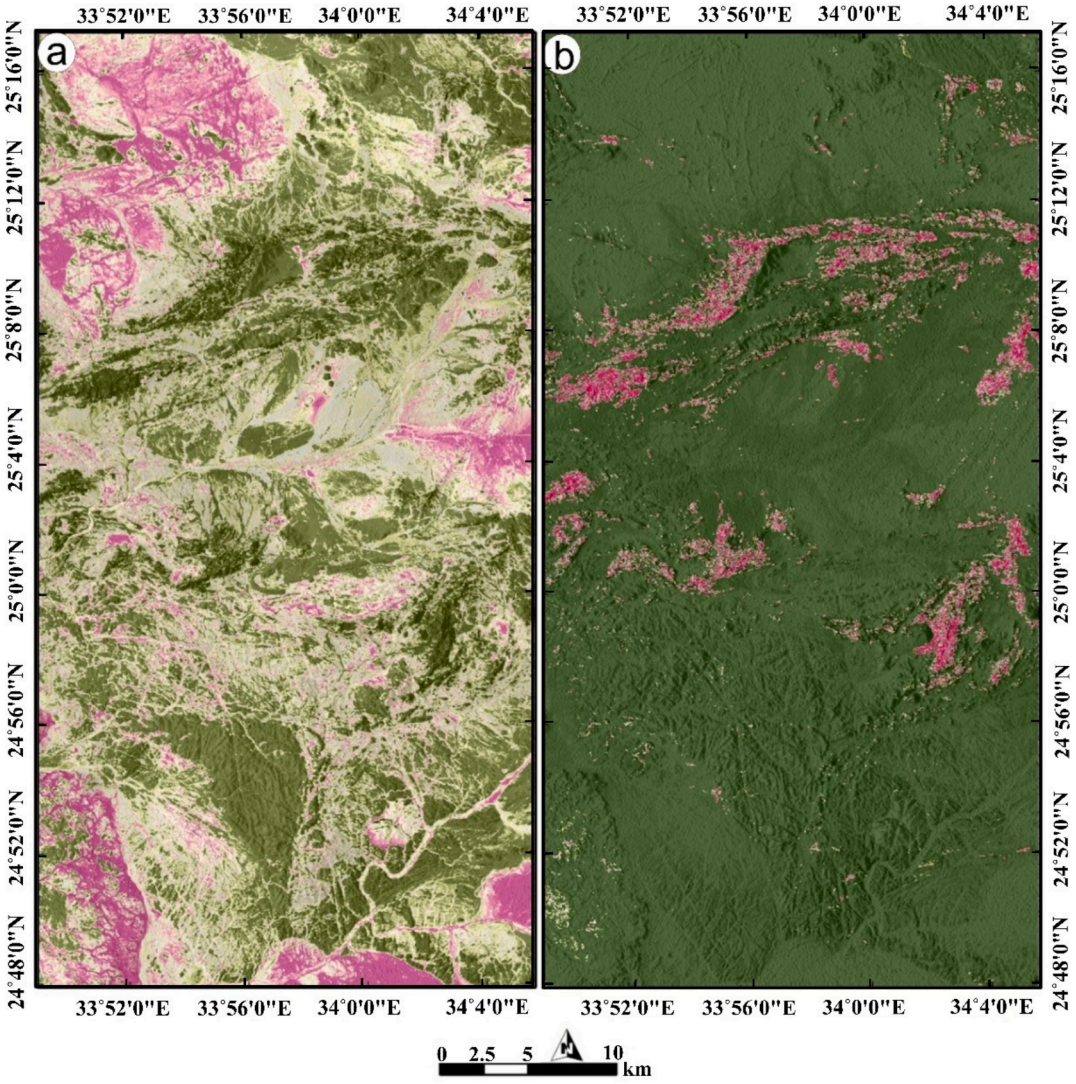

Fig. 12. Pseudocolor images displaying SMACC abundances of a) Endmember 1 emphasizes bright pixels corresponding to granitic rocks and their weathering products (in pink), and b) Endmember 26 delineates serpentinite rocks (in pink). (For interpretation of the references to color in this figure legend, the reader is referred to the web version of this article.)

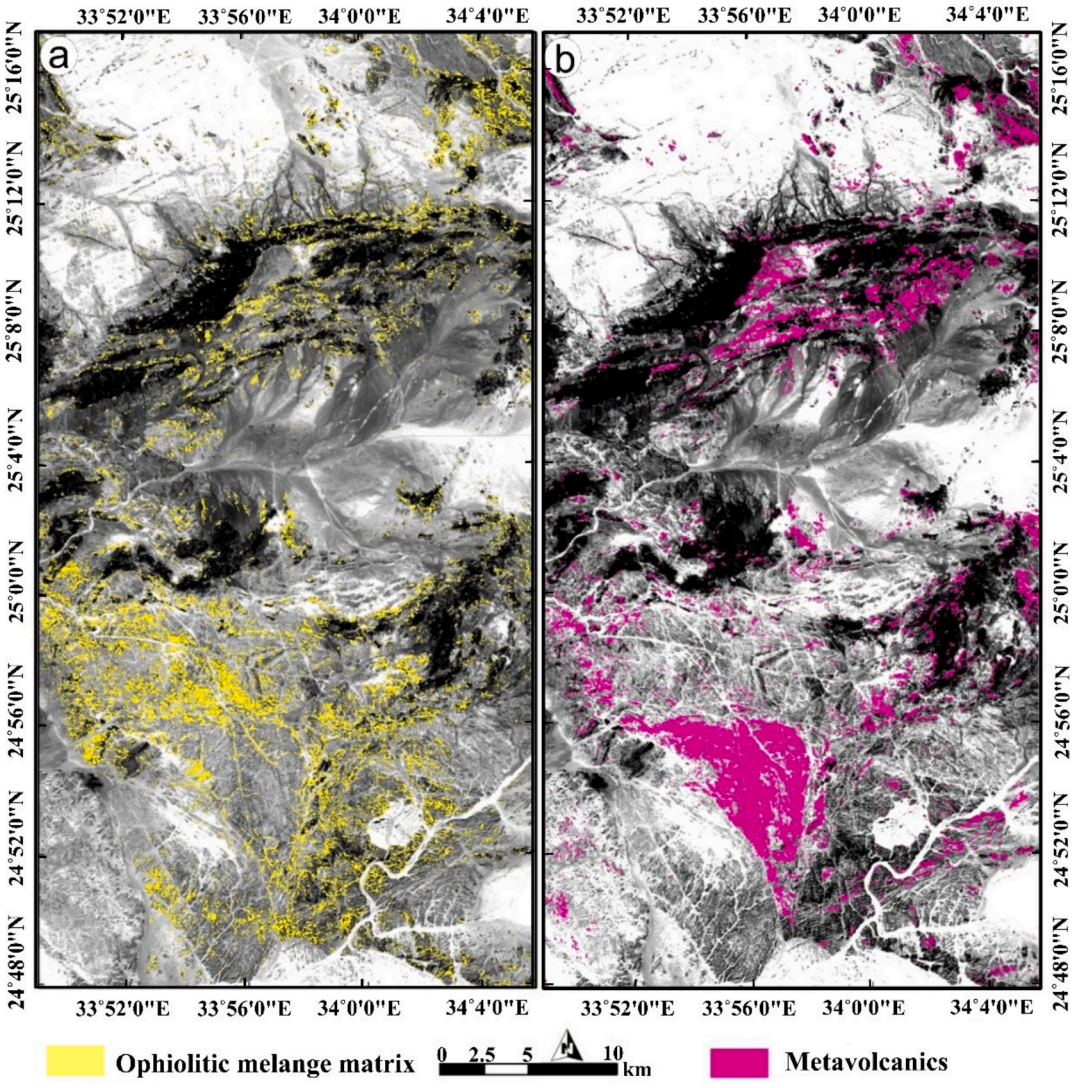

Fig. 13. SMACC abundances of a) Endmember 19 separating the mélange matrix represented by volcaniclastic metasediments, and b) Endmember 7 delineates island arc metavolcanics within the study area.

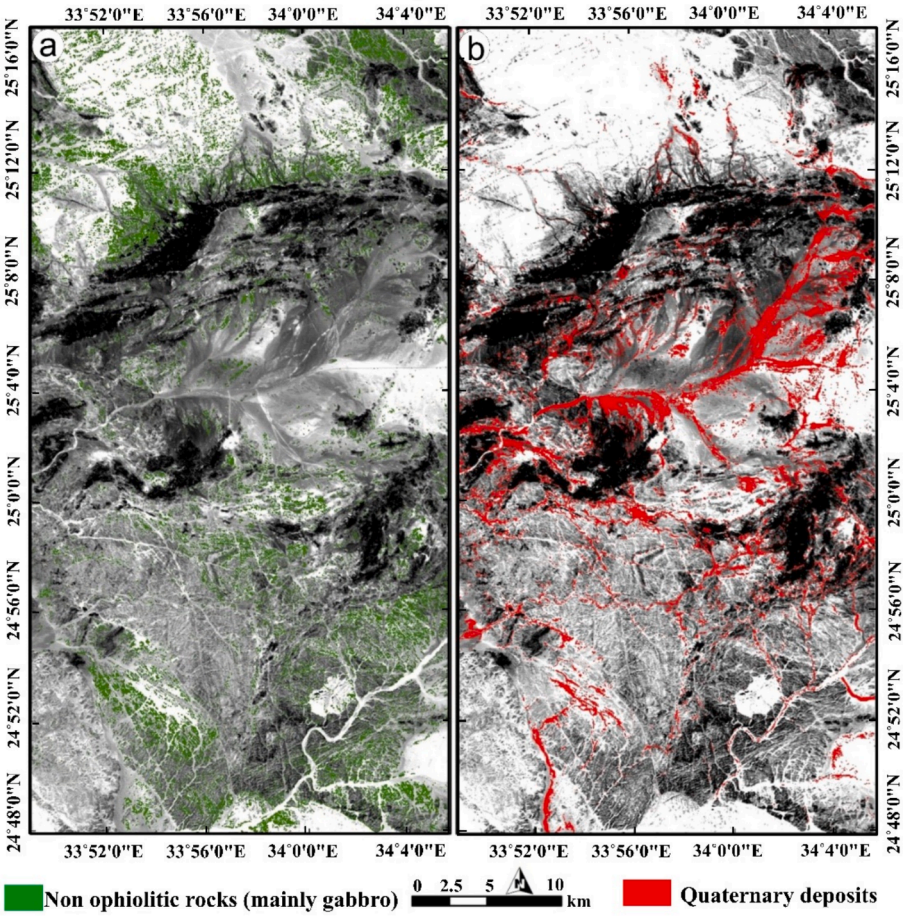

Fig. 14. SMACC abundances of a) Endmember 29 separating non ophiolitic rocks within the study area, and b) Endmember 28 delineates the main quaternary deposits within the study area.

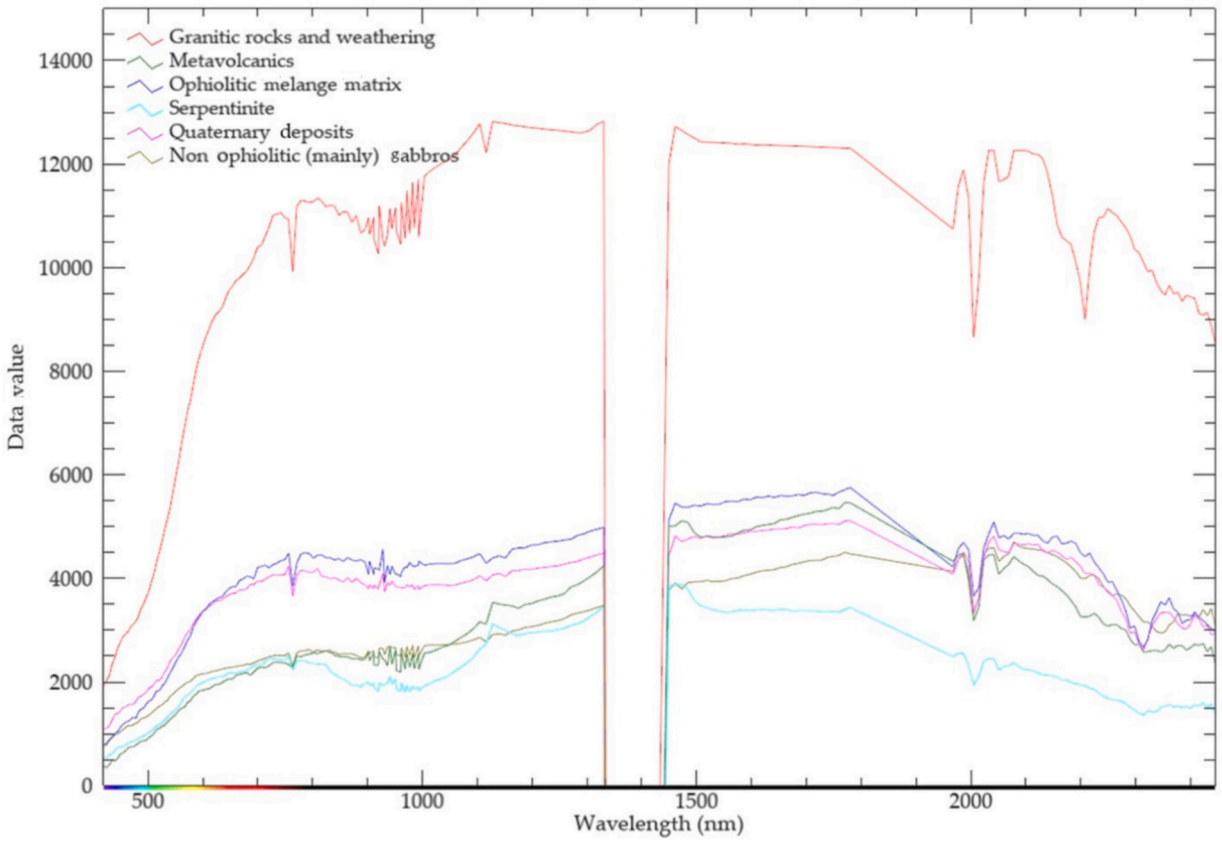

Fig. 15. Variations in endmember spectral curves reflect the diverse chemical and mineralogical compositions of the studied lithologies, facilitating their separation through EnMap data SMACC analysis.

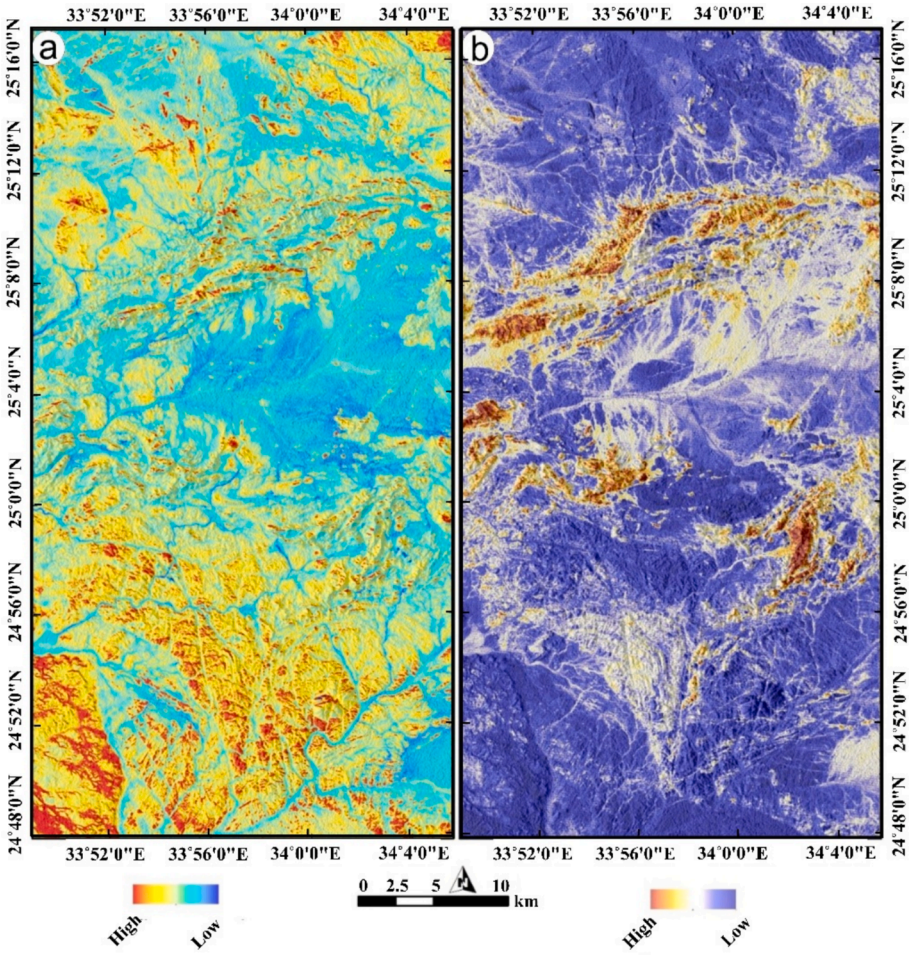

Fig. 16. Illustrating the key hydrothermal alteration pattern in the study area, with a) iron-bearing minerals highlighted using wavelengths (nm) of 666.63 (b48) / 491.78(b16), and b) OH-bearing alteration emphasized via wavelengths (nm) of 1609.02 (b150) / 2445.30 (b224).

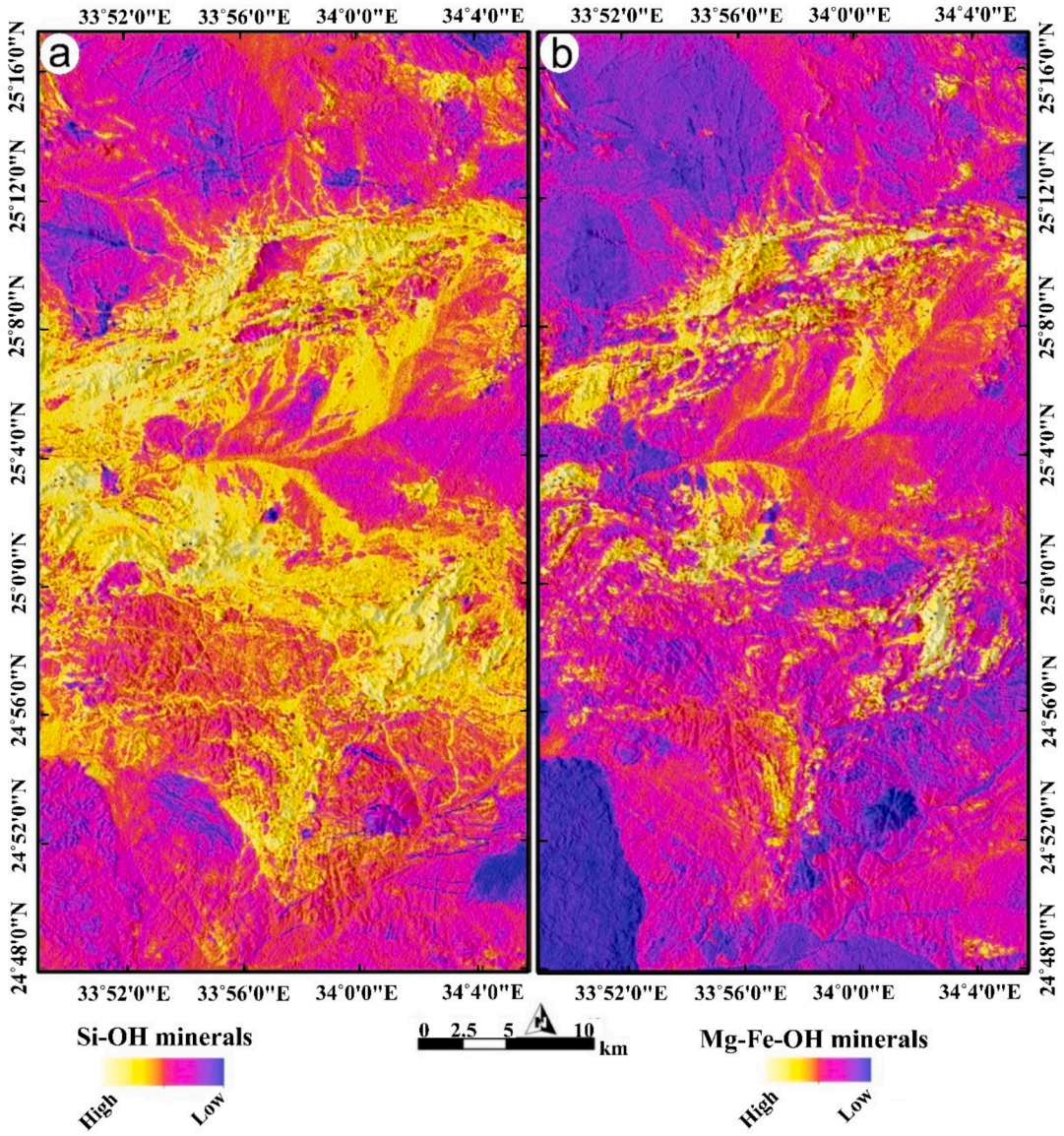

Fig. 17. Showcasing EnMap's ability to identify Si-OH minerals and pinpoint the distribution of Mg-Fe-OH minerals within this category using the expressions (a) (b194 + b209)/b201 and (b) (b201 + b218)/b209, respectively. The corresponding wavelengths (nm) are as follows: b194: 2207.8, b201: 2265.79, b209: 2330.05, and b218: 2400.00.

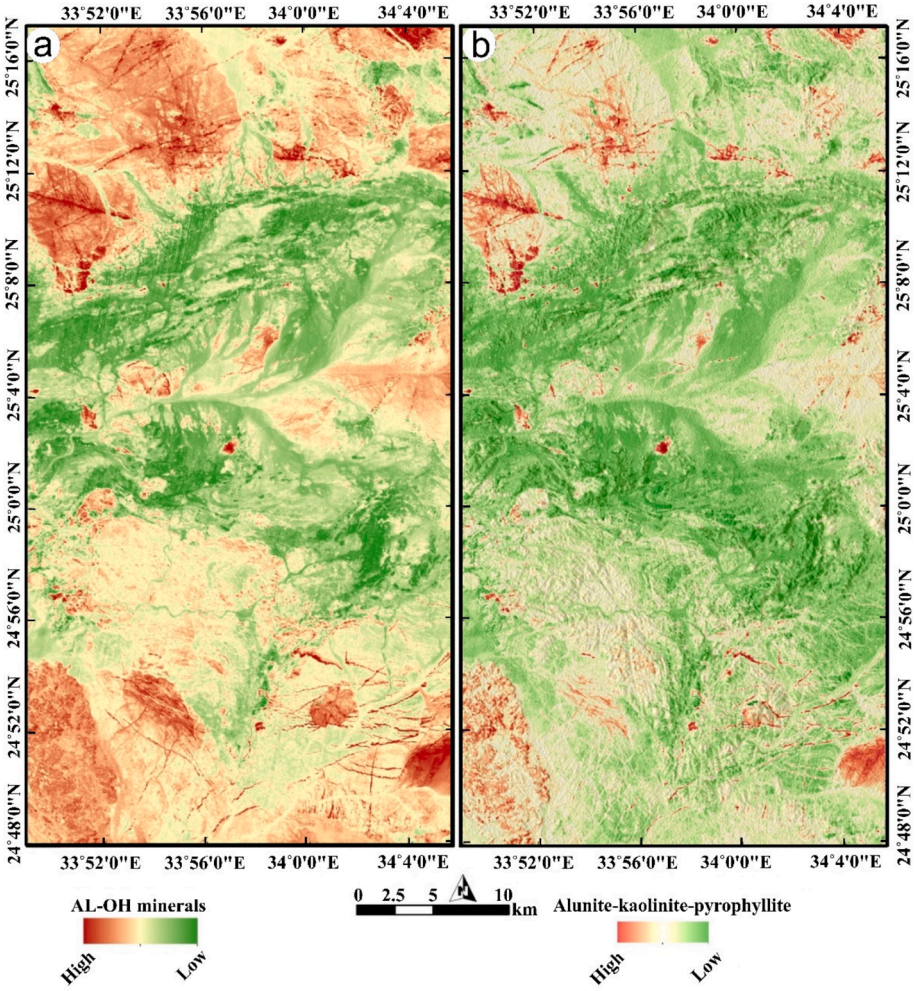

Fig. 18. Pseudocolor images revealing the distribution of Al/Fe-OH-bearing rocks using the expression of (a) (b189 + b201)/b194, predominantly found in acidic rocks and Nubian sandstone. This sheds light on the potential richness of Nubian sandstone in Al-bearing ores (e.g., bauxite). b) The distribution of alunite, kaolinite, and pyrophyllite within the study area using the expression of (b154 + b201)/b194. The corresponding wavelengths (nm) are as follows: b154: 1653.00, b189: 2165.47, b194: 2207.86, and b201: 2265.79.

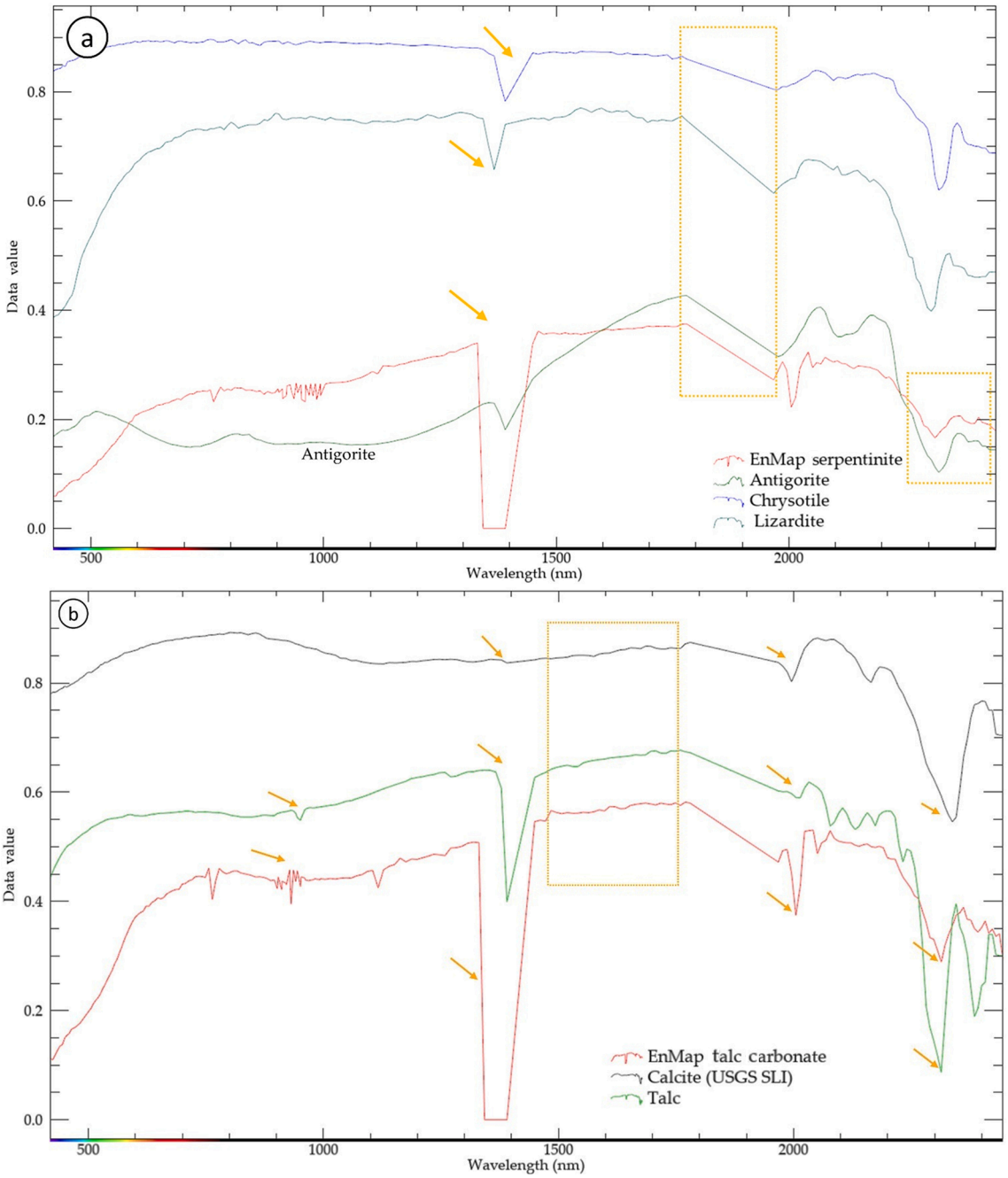

Fig. 19. Spectral correlation between a) EnMap signatures of serpentinite rocks and serpentine mineral curves, highlighting predominantly antigoritic composition for the studied rocks. b) Talc carbonate rocks show harmony with their main mineralogical composition (talc and calcite curves).

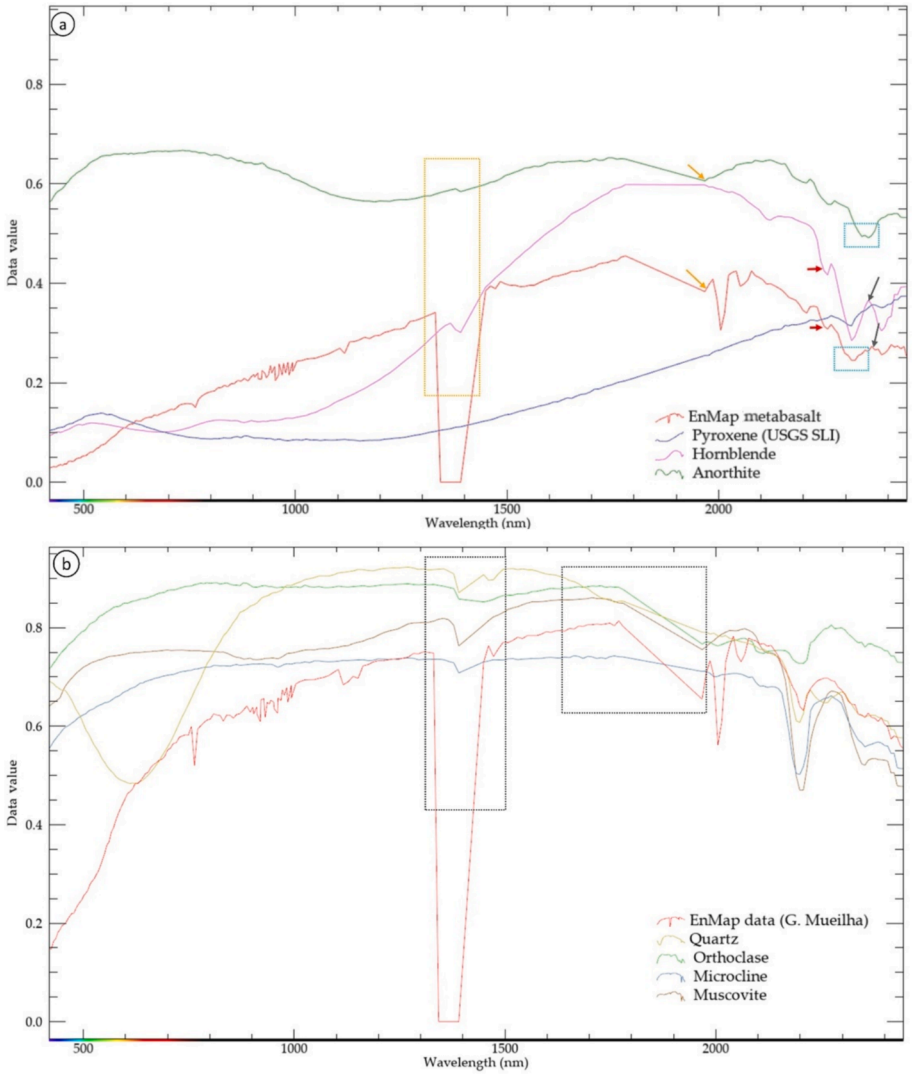

Fig. 20. Spectral correlation between EnMap signatures and key minerals from a) basic metavolcanics and b) Granitic rocks, suggesting the EnMap spectral curve combines features of these rock-forming minerals.

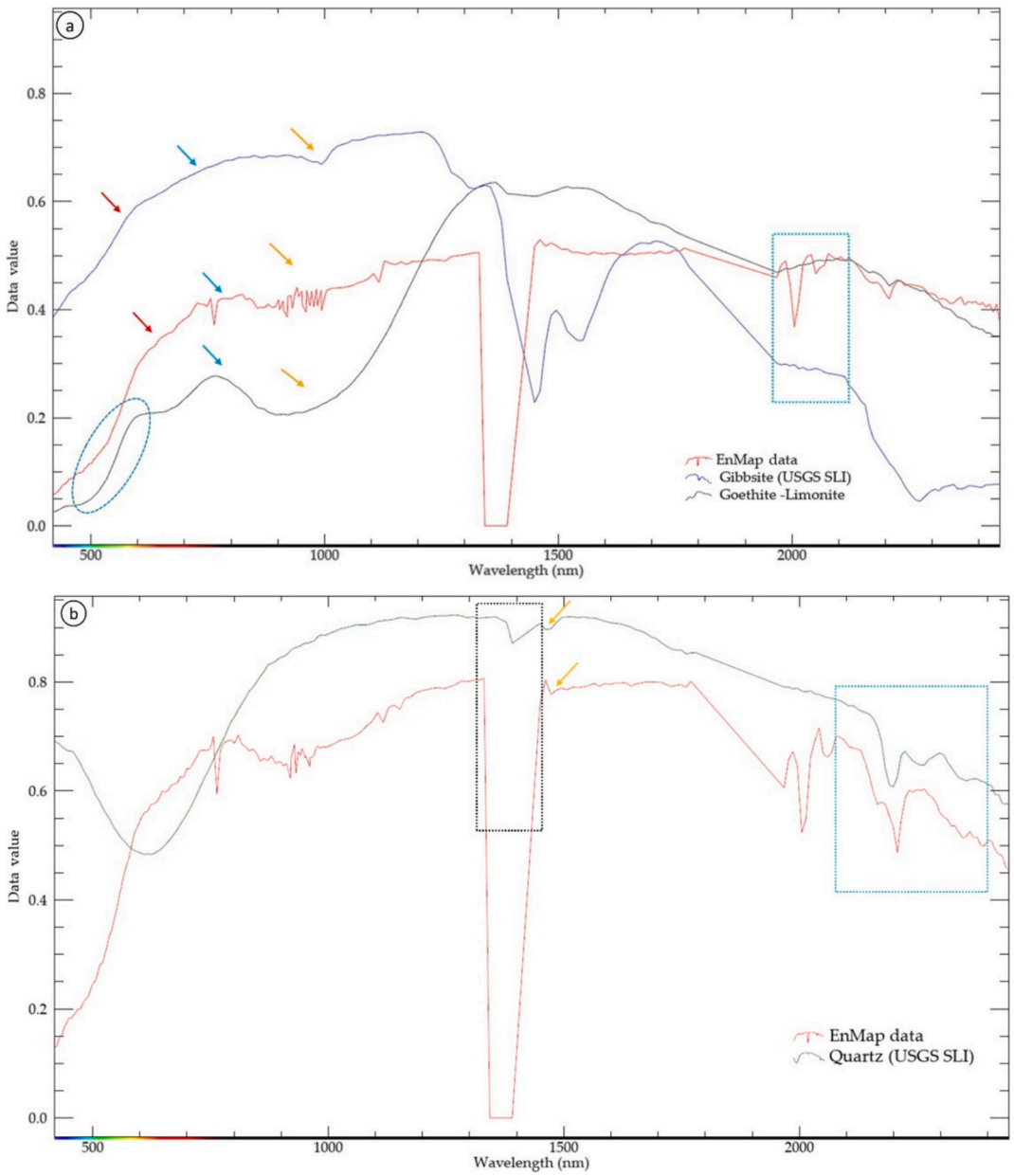

Fig. 21. Spectral correlation between EnMap signatures of a) Nubian Sandstone with goethite and gibbsite, and b) Quartz plugs, highlighting a significant resemblance between the curves.

representations with EnMap data (Fig. 11). This strongly recommends the use of UMAP with EnMap for future applications.

4.2. SMACC analysis

However, while image processing techniques (e.g., PCA and ICA) delivered reasonable findings, a more detailed spectral analysis was performed to ensure the meticulous delineation of each rock unit in the studied terrain. The Sequential Maximum Angle Convex Cone (SMACC) approach was applied to identify the main spectral endmembers and their distribution throughout the study area. SMACC begins by identifying the brightest pixel in the image, then searches for the one that is most different from it. This process continues, with SMACC identifying the next most distinct pixel from those already selected until it either encounters a pixel that has already been included or reaches a specified number of endmembers.

Confirming UMAP spectral separability, SMAAC endmembers were able to discriminate most of the studied rock units. The first SMACC endmembers clearly highlighted the brightest pixels, indicating the weathering and alteration products of granitic bodies within the study area (Fig. 12a). Adequate delineation of serpentinite blocks was achieved through SMACC endmember 26 in our analysis (Fig. 12b). Investigating the abundances of these endmembers highlighted the accuracy of this spectral analysis in separating the rock units. For instance, in Fig. 12b, only serpentinite blocks of Gabal Um Salatit, Um Salim, the eastern part of Gabal Barramiya, and the southwestern part of Wadi Beizah were delineated without even highlighting their associated listvaenite and talc carbonate rocks depicted in Fig. 7a. These serpentinite blocks form the main dismembered ophiolitic bodies (tectonic mélange of allochthonous blocks of serpentinite) that, together with the mélange matrix, constitute the ophiolitic mélange within the study area.

For the first time, SMACC analysis of EnMap data was capable of separating the mélange matrix through the abundances of endmember 19, as shown in Fig. 13a. The distribution of these volcaniclastic

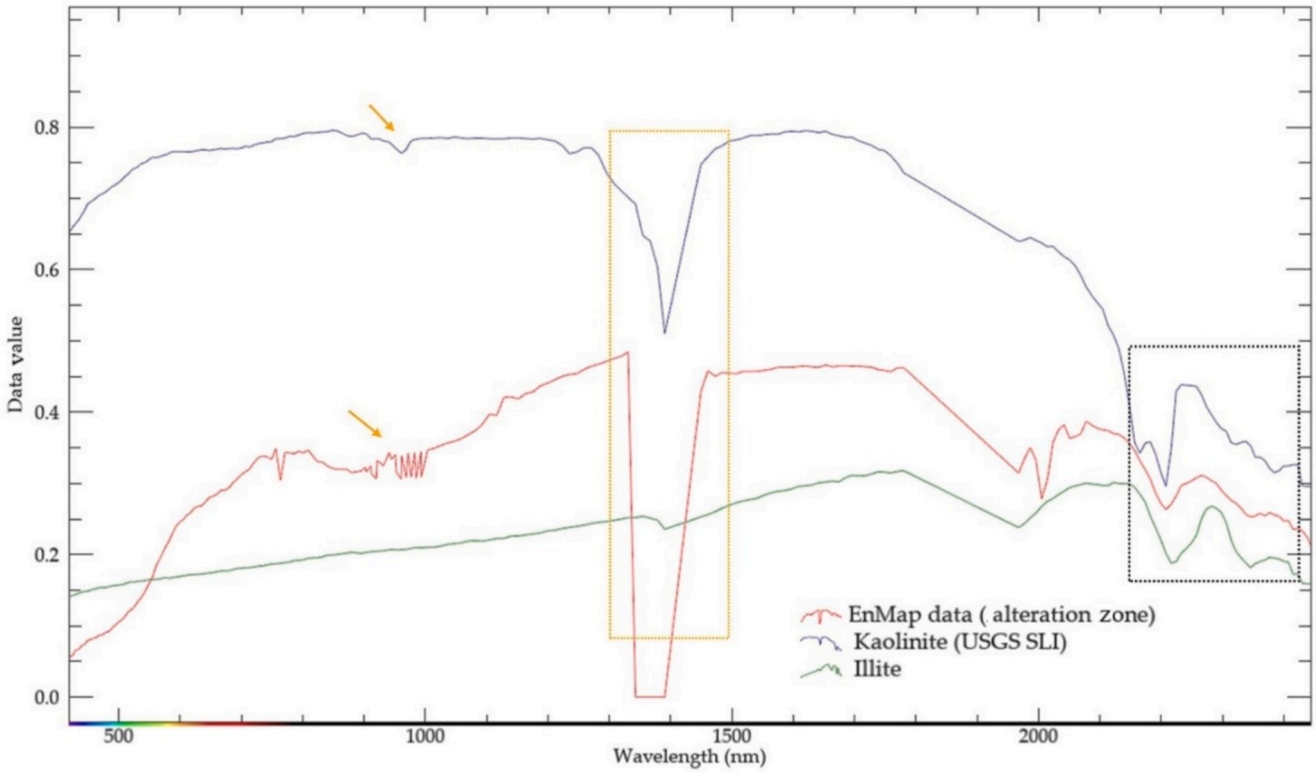

Fig. 22. Spectral correlation between EnMap signatures and key mineral constituents of the altered zone illustrates the effective combination of mineralogical curves features in the EnMap data.

metasediments was spatially associated with serpentinite blocks without any confusion with such rocks or with island arc association within the study area. This task is particularly challenging when using multispectral or even hyperspectral data because the mélange matrix rocks contain various components and are described as mixed rocks comprising blocks with diverse ages and origins (Kusky et al., 2020; Shebl et al., 2022). As mixing can occur across multiple scales, potentially even beneath the resolution of individual pixels (Kusky and Bradley, 1999; Shebl et al., 2022), accurately separating this unit poses a significant challenge. Consequently, the utilized approach did a commendable job by reasonably identifying this complicated rock unit, as shown in Fig. 13a, and highlights the usefulness of EnMap data for future complicated geological applications.

Fig. 13b depicts the spatial distribution of island arc metavolcanics within the study area, delineated by the abundance of endmember 7. This rock unit represents one of the most complex lithologies encountered in the study region. Comprised of metamorphosed calc-alkaline volcanics with an andesite-dacite composition (Shebl et al., 2022; Zoheir et al., 2019), the metavolcanic rocks exhibit a diverse range of lithofacies, including interrelated pyroclastic volcanic tuffs and breccias. Within the study area, these metavolcanic rocks encompass a blend of metabasalt, basaltic *meta*-andesite, and dacitic tuffs and agglomerates, occasionally interspersed with carbonate fragments. In the vicinity of Wadi Dungash, the island arc rocks predominantly comprise medium- to fine-grained metabasalt and *meta*-andesite, occurring in either massive or foliated forms (Abdel-Karim et al., 1996; Zoheir et al., 2019). Despite the compositional complexity and spatial proximity between the ophiolitic mélange matrix (volcaniclastic metasediments) and island arc metavolcanics, their distribution accurately aligns with our field investigations and previous studies.

Other rock units successfully separated by SMACC include metagabbroic rocks within the study area. Their distribution is depicted in Fig. 14a through endmember 29 abundances. Metagabbroic rocks are primarily found along the northeastern and central (around Wadi Beizah along the main east–west asphaltic road crossing the area) parts of the map, as well as in the southern part of the map, either around Gabal Mueilha granitic rocks or beneath the main island arc blocks at the southwestern part of the study area. Additionally, the distribution of Quaternary deposits within the study area is illustrated through the endmember 28 distribution in Fig. 14b. These deposits are primarily targeted for placer deposits within the study area and already exhibit some artisanal mining activities, as verified through our field observations. For future studies in similar terrains, the spectral curves of all these endmembers are presented in Fig. 15, demonstrating how they differentiate from each other. These spectra offer insights into separating such complex terrains using EnMap data or other similar hyperspectral products through the identification of their absorption bands.

4.3. Hydrothermal alteration mapping

EnMap spectral analysis has delivered a precise delineation of the complicated lithological features within the study area. Furthermore, EnMap data were utilized for further delineating and characterizing hydrothermal alteration patterns. Our findings indicate that the exposed lithologies in the region are influenced by iron-bearing and OH-bearing alteration minerals. For instance, Fig. 16a illustrates the distribution of iron-bearing minerals within the study area based on the VNIR band ratio of b48/b16. This figure reveals an extensive presence of iron oxides across various lithologies, including Nubian sandstone (located in the southwestern corner of the map), metagabbros, and metavolcanics in the southern part of the study area, along with scattered red dots indicating hydrothermally altered zones or already existing random mining areas. On the other side, a SWIR band ratio of b150/b224 was employed to delineate OH-bearing alteration minerals within the study area, as depicted in Fig. 16b. This figure exclusively highlights serpentinite rocks, along with some metavolcanics, and successfully identifies portions of artisanally mined areas.

Due to EnMap's abundant spectral information, a precise

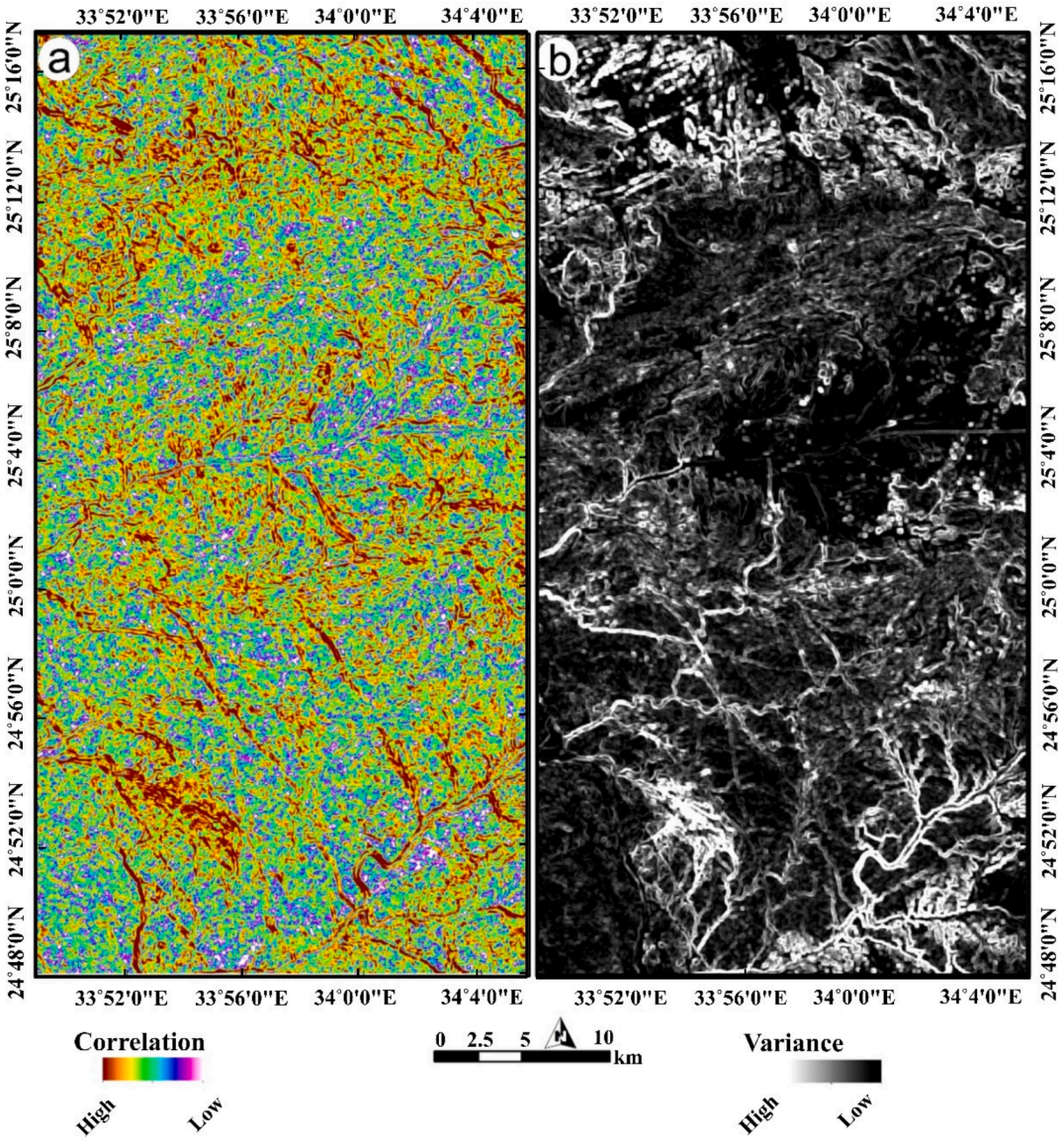

Fig. 23. Key structural elements identified through textural analysis of EnMap data: (a) Correlation, revealing the dominance of NW-trending structural features. (b) Variance, highlighting NE-trending features, predominantly represented by structurally controlled wadis.

characterization of the hydrothermal alteration pattern was conducted. For example, the expression (b194 + b209)/b201 was utilized to differentiate Si-OH minerals within the study area. Fig. 17a illustrates the distribution of hydrous silicate-bearing rocks and carbonates predominantly in the central part of the study area, primarily confined to serpentinites and their associated talc-carbonates, as well as significant portions of metavolcanics and volcaniclastic metasediments. It is essential to emphasize that this band algebra distinctly highlights granitic rocks within the study area in blue, indicating a lower concentration of Si-OH minerals compared to other lithologies. Further investigations and in-depth analyses were conducted to specify Mg-Fe-OH minerals from the broad category of Si-OH minerals. To achieve this goal, the band math of (b201 + b218)/b209 was applied, successfully distinguishing Mg-Fe-OH minerals (Fig. 17b) from Si-OH minerals. As anticipated, Mg-Fe-OH minerals within the study area are mainly represented within serpentinite rocks. It is noteworthy that granitic rocks are still depicted in a deep blue color, indicating their depletion of Mg-Fe-OH minerals compared to serpentinite rocks. Comparing the areal extent of Fig. 17a and Fig. 17b highlights the effectiveness of the utilized band math in specifying Mg-Fe-OH minerals from Si-OH minerals.

Regarding the discrimination of acidic rocks (mainly granitic rocks within the study area), we utilized a band math equation of (b189 + b201)/b194 to identify Al/Fe-OH-bearing rocks (Fig. 18a). This combination effectively highlighted all granitic materials within the study area, whether they were fresh, weathered, or altered. Consequently, this equation could be employed to pinpoint minerals such as sericite, muscovite, illite, and smectite (Fig. 18b). Notably, this band expression showcased the Mueilha granite and its associated dykes in the southeastern part, as well as the presence of Nubian sandstone in the southwestern corner, marked in red to denote higher Al/Fe-OH content. This indicates further analysis to investigate Al-bearing ores (e.g. bauxite) within the Nubian sandstone and along its contact with the Precambrian rocks. In the central region of the study area, weathering products derived from granitic sources were observed along wadis, also highlighted in red. Furthermore, in the northern part of the study area, all granitic content and its weathering products were discerned (e.g., Gabal El Rukham). To accurately specify areas of true alteration zones within these acidic lithologies, a band expression of (b154 + b201)/b194 was applied, revealing smaller areas predominantly characterized by the dominance of minerals like alunite, kaolinite, and pyrophyllite.

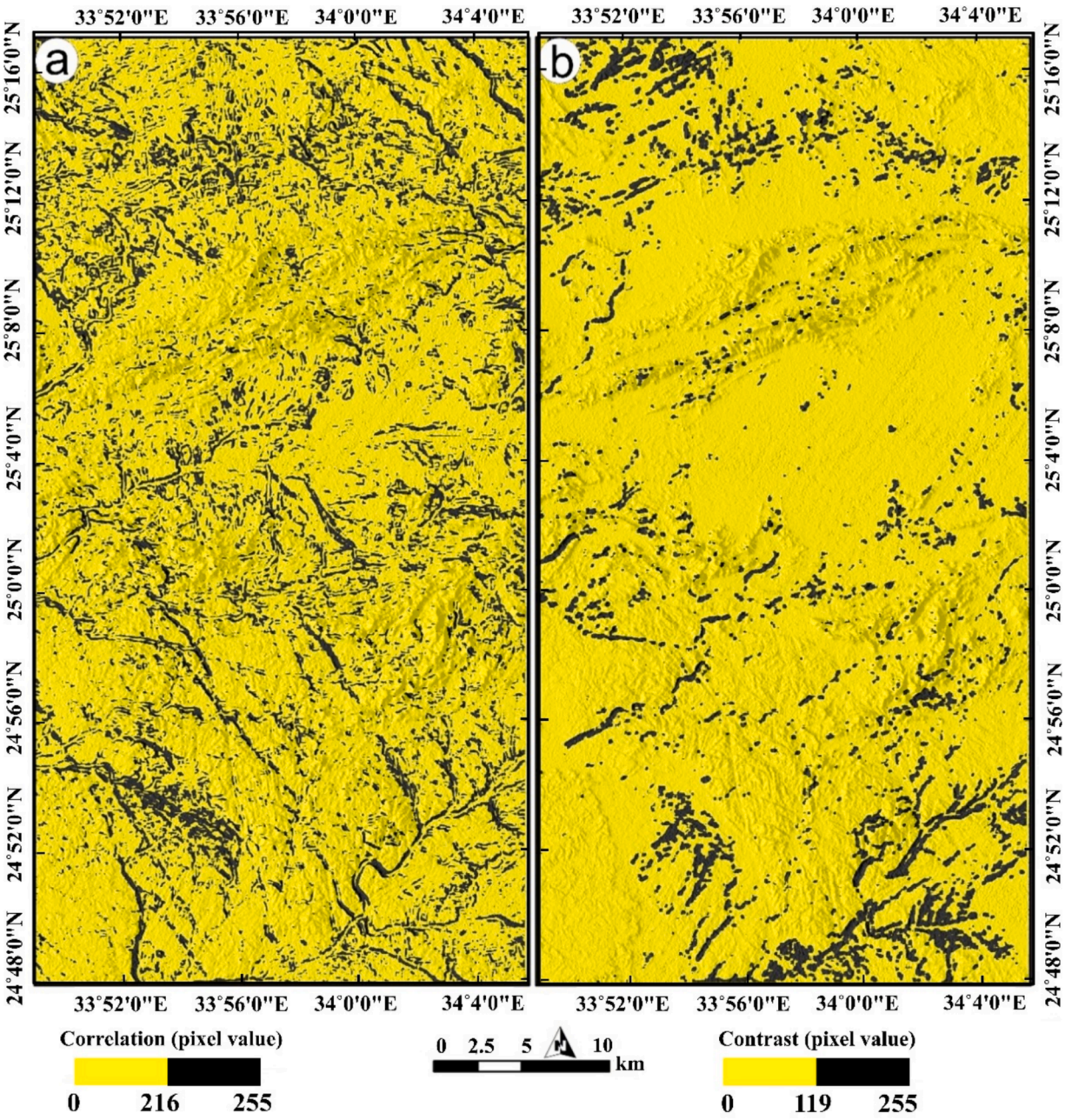

Fig. 24. Visualization of primary structural elements depicted as black pixels, derived from (a) Correlation and (b) Contrast values.

4.4. Quantifying spectral analysis

This section explores the use of EnMap spectral analysis to identify a rock type (mineral associations) or certain minerals by examining their unique absorption signatures. Such determinations largely depend on the absorption feature's specific location and intensity at given wavelengths within the VNIR-SWIR spectrum. For instance, the detection of electronic transitions in the VNIR spectrum, particularly due to crystal field effects impacting elements like Fe^{2+} and Fe^{3+}, highlights the presence of iron-bearing minerals (Bishop, 2019; Douglas et al., 2022; Shebl et al., 2023a; van der Meer et al., 2018). This is attributed to changes in the electronic states of iron within these minerals. Furthermore, as (Bishop, 2019; Shebl et al., 2023a) highlighted, the phenomenon of vibrational absorption occurs when molecular bonds within a mineral are excited from a lower to a higher energy state. This excitation leads to the absorption of light at wavelengths that correspond to these specific energy jumps. Such a process is notably responsible for the way hydroxyl-bearing minerals absorb light within the SWIR region.

The normalized EnMap data spectra were meticulously compared to the resampled U.S. Geological Survey (USGS) spectral library, a process conducted manually to discern similarities in both the location and morphology of absorption features. Carefully chosen sites for spectral comparison were selected based on our comprehensive field observations, emphasizing the EnMap data's efficacy in accurately representing spectral compositions compared to the reference spectra.

Fig. 19a compares the EnMap spectral signature of serpentinite rocks exposed within the study area with the spectral characteristics of serpentine minerals (antigorite, chrysotile, and lizardite). An overall correspondence (indicated by the arrows and boxed annotations) with the spectra of the three minerals is noticeable, particularly in the absorption features in the SWIR range typical of OH-bearing minerals. However, the closest match is observed with antigorite, where the absorption bandwidth (around 2300 nm) is slightly broader than that exhibited by chrysotile and lizardite. Additionally, there is a nearly exact

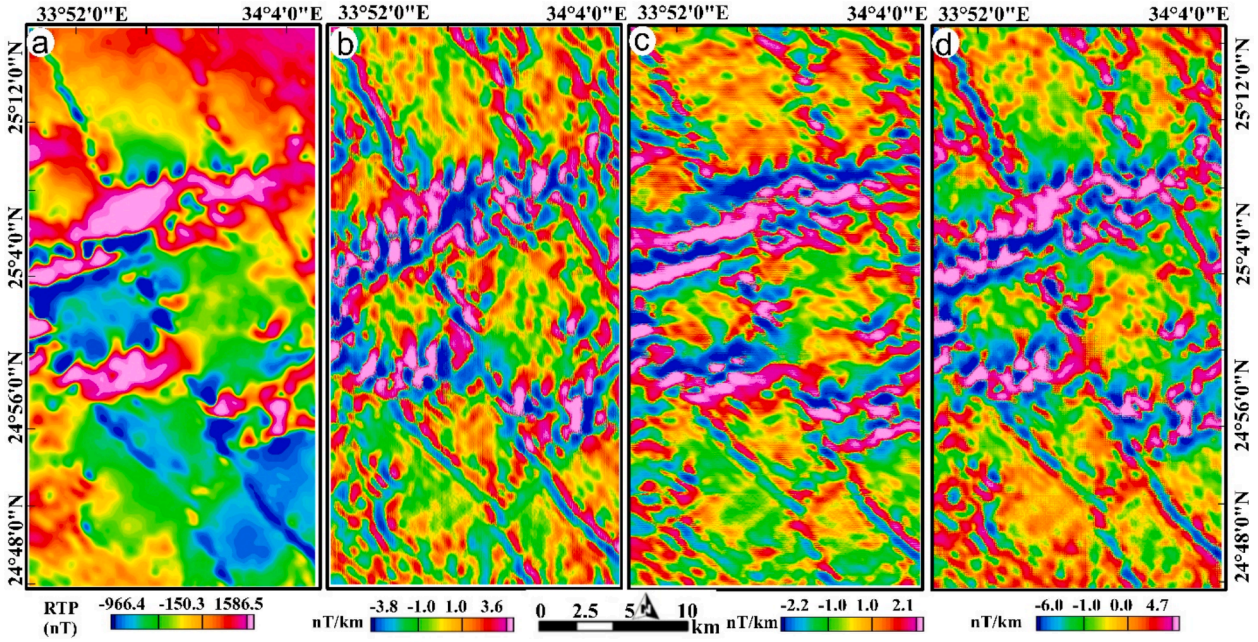

Fig. 25. Airborne geophysical results a) RTP map, b) Derivative in x-direction map, c) Derivative in y-direction map, d) First vertical derivative map.

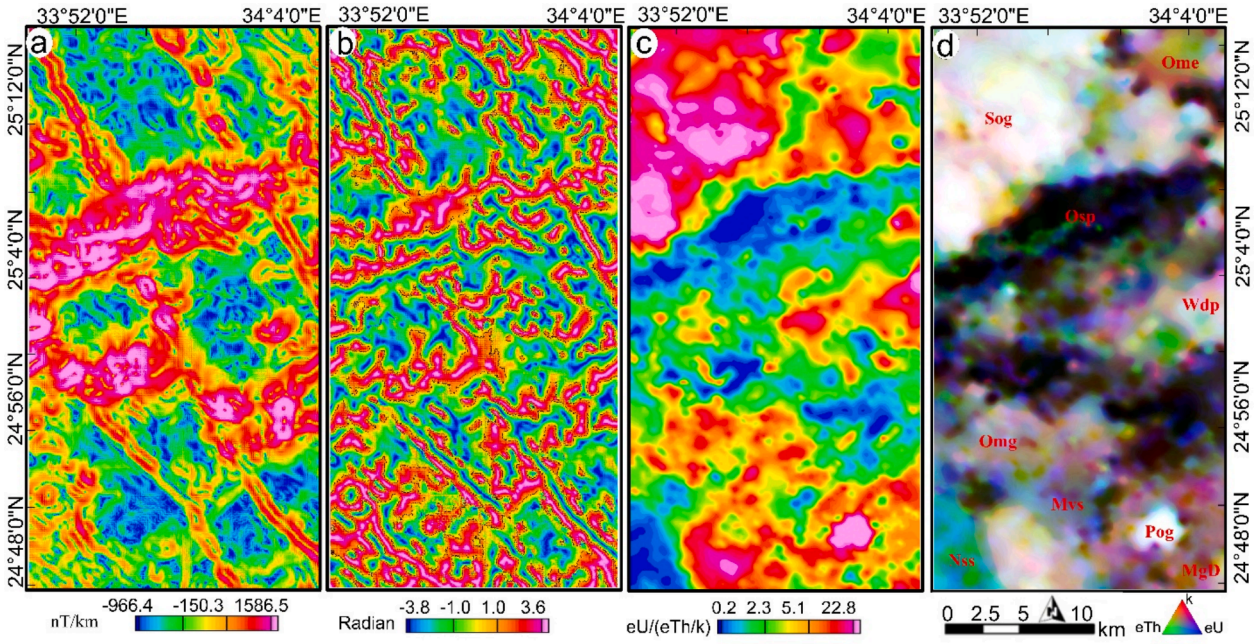

Fig. 26. Airborne geophysical results a) THD map, b) TDR map, c) F-parameter map, d) Ternary composite map. Ophiolitic serpentinite (Osp), volcaniclastic metasediments as an ophiolitic mélange matrix (Ome), metavolcanics (Mvs), metagabbro-diorite (MgD), *syn*-orogenic granite (Sog), post-orogenic granite represented by mueilha granite (Pog), nubian sandstone (Nss), and wadi deposits (Wdp).

representation of the antigorite spectral curve with the EnMap curve within the range of 2300 nm to 2450 nm. This finding is consistent with our petrographic investigations of samples from that location, where the serpentine rocks are primarily composed of antigorite. Serpentinite rocks are predominantly linked with talc carbonates in the studied terrain. Consequently, we assessed the efficacy of EnMap data spectra in identifying talc carbonates by comparing their spectra with the reference spectra of talc and calcite (Fig. 19b). The comparison distinctly illustrates that EnMap spectral representation effectively captures the combined spectral information from talc and calcite (as indicated by the arrows and boxed annotations). This demonstrates a direct application of utilizing spectral information to identify rock types based on their mineralogical associations.

Similarly, we analyzed basic metavolcanics (Fig. 20a) and granitic rocks (Fig. 20b) by comparing their EnMap spectral representations with those of their essential minerals. While some degree of matching is evident and deemed acceptable as an overall representation of these lithological compositions, it is worth noting that achieving a typical match when comparing such spectrally complex lithologies is challenging. For example, in the study area, basic metavolcanics encompass a range of compositions including metabasalts and andesitic metabasalts. These lithologies contain numerous accessory minerals, in

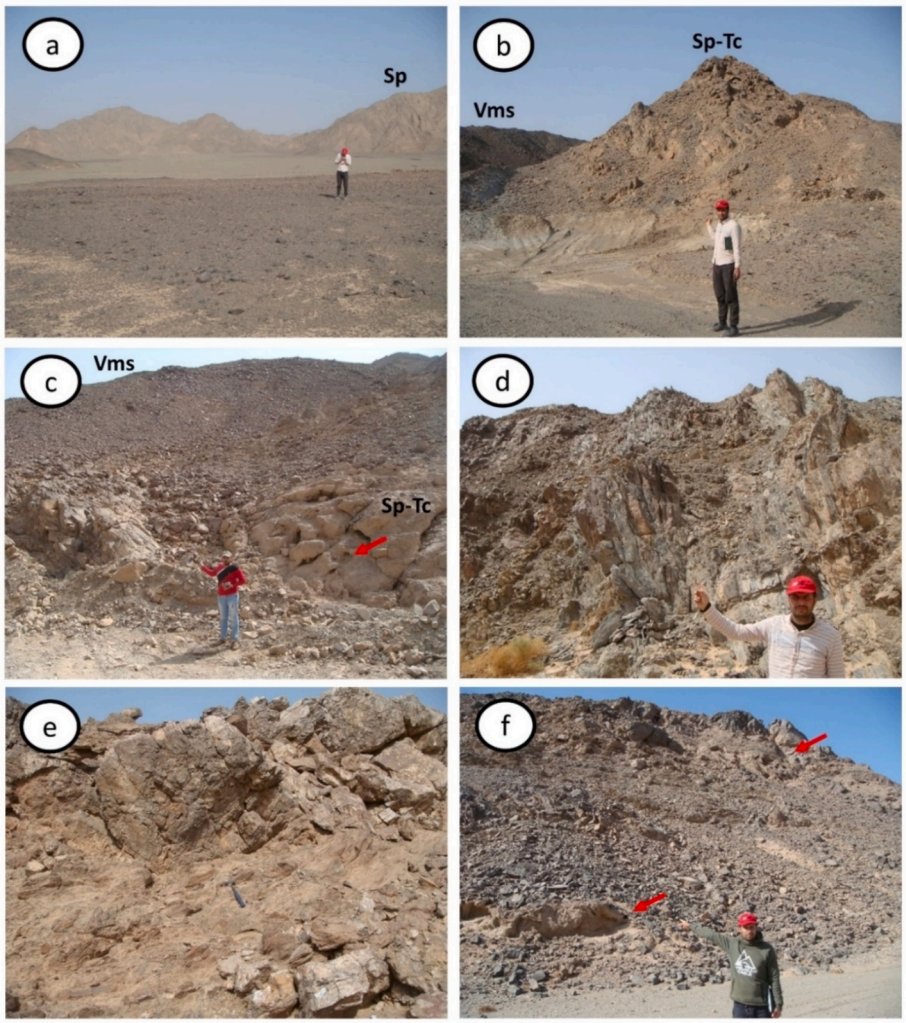

Fig. 27. Field photographs showing the main geological features of serpentinites and their related rocks within the study area. (a) A panoramic view of Gabal Um Salatit serpentinite (b) Large serpentinite-talc carbonate blocks embedded within a matrix of volcaniclastic metasediments, (c) Close-up view of serpentinite-talc carbonate blocks showing their cavernous structure (see the arrows). (d) Intensively sheared serpentinite-talc carbonate rocks, (e) Listvenization, a distinct alteration process in serpentinites, (f) alteration of serpentinites (see the arrows) to talc carbonate rocks (buff color). Sp-Tc for serpentinite-talc carbonate, and Vms for volcaniclastic metasediments.

addition to the essential ones, which significantly influence their spectral representations. Furthermore, the impact of metamorphism (resulting in metabasalts rather than fresh basalts) and desert varnish may also contribute to discrepancies observed in the EnMap spectral curve compared to the provided reference spectra of essential minerals.

In the case of representing granitic rocks, Gabal Mueilha granite was chosen for that analysis. A discernible correspondence between the main rock-forming minerals and the EnMap spectral representation is evident. For example, quartz exhibits a known spectral absorption band at 1436 nm, which is distinctly represented within the absorption range of the EnMap spectra. Additionally, an absorption wavelength of around 2200 nm is observed in the EnMap spectra, considered a characteristic absorption feature for muscovite, quartz, and K-feldspars, which are recognized as essential minerals within Mueilha granite.

All the preceding examples highlighted how effectively EnMap data can aid in accurate lithological mapping based on the spectral characteristics of rock-forming minerals (mineral associations). Furthermore, specific minerals, such as hydrothermal alteration minerals, were successfully analyzed and detected through EnMap spectral data analysis. For instance, in the southwestern corner (near the Nubian sandstone) of the map, EnMap data spectral curves were scrutinized and compared with those of goethite and gibbsite (Fig. 21a). Examination of these curves distinctly revealed the identification of goethite and gibbsite, particularly by correlating their VNIR spectral signatures with the EnMap data. Notably, a concordance among the three curves is observed within the wavelength ranges of 450 nm to 600 nm, alongside a prominent absorption band around 950 nm, characteristic of both minerals and evident in the roughness of the EnMap spectral curve. Additionally, in the SWIR region, an absorption band indicative of Al-OH is evident in all three curves.

It is important to emphasize that due to the coarser spatial resolution of the EnMap data, a single pixel may comprise a mixture of goethite, gibbsite, and even quartz (from Nubian Sandstone), along with other weathering products. This may account for some discrepancies among these curves; however, the characteristic absorption troughs remain prominent for these minerals in the EnMap data. This study also suggests further exploration for bauxite ores, as identified by one of their key minerals, gibbsite. Based on our findings, the location of these ores is confined to the southwestern corner of the study area, mainly attributed to the contact between the Nubian sandstone and the Neoproterozoic rocks. Specific mineral spectral analysis was further conducted on quartz by juxtaposing the EnMap spectra from quartz plugs within the study area with the reference USGS spectral curve (Fig. 21b). Additionally, an alteration zone spectral signature was established using EnMap data,

Fig. 28. Field photographs showing, (a, b) Highly dissected arc metavolcanics, (c) Highly deformed metagabbro-diorite rocks, (d, e) Highly sheared granite intrusions, (f) Post-tectonic Mueilha granite intruded into metagabbros with a distinct sharp contact.

revealing a notable alignment (as indicated by arrows and boxes) with kaolinite and illite (Fig. 22), which were identified during fieldwork at that site.

In addition to hydrothermal alteration analysis, EnMap data was subjected to textural analysis using a 7 × 7 kernel to highlight the primary structural features within the study area. This second-order statistical analysis involved calculating several attributes, including mean, variance, homogeneity, contrast, entropy, and correlation. The results demonstrated that correlation (Fig. 23a and 24a), variance (Fig. 23b), and contrast (Fig. 24) were the most effective in detecting structural features, primarily revealing NW- and NE-trending structures within the terrain.

4.5. Geophysical data findings

The main objectives of the airborne geophysical analysis in our study are to drastically emphasize its role in mapping hydrothermal alteration tracts and different lithological units. This purpose is achieved by the precise interpretation of the subsequent processed maps. Initially, the TMI grid map (Fig. 4a) was reduced to magnetic pole (Fig. 25a) to place magnetic anomaly over their sources via applying Fast Fourier transform filter and the inclination and declination parameters of the magnetic field were 32.8 north and 1.9 east respectively. The RTP map of the study area (Fig. 25a) characterized by high magnetic anomaly (pink color) correlated to ophiolitic rocks while low to medium magnetic sources (blue −green and yellow brown colors) related to post-orogenic granite, metavolcanics and sedimentary rocks. It is worth noting that the causative bodies are mainly oriented in NW and NE directions. The structural features controlling the mineralization in the area were depicted by applying the previously mentioned gradient techniques on the RTP map. In detail the horizontal and vertical derivatives (Fig. 25b) clearly revealed the textures and highlighted discontinuities of anomaly patterns. Also, the maxima of the total horizontal gradient (Fig. 25c) showed the contact locations, while the horizontal and vertical edges of the concealed magnetic bodies revealed by applying tilt angle (Fig. 25d) on the RTP. To sum up, the area was highly structured and deformed and the main structural trends controlling the occurrences of mineralization are NW and NE directions as clearly seen via gradient maps. The radioelements concentration maps (Fig. 4) are well correlated to the lithological units in the area where high concentrations of K, eTh and eU are associated with granite rocks while ophiolitic ones show low concentrations. Ratios of the radioelements are very important for reducing the effect of exposer amount and soil water content. Based on the basis of the ratios the hydrothermally altered area is deduced from the F-parameter map (Fig. 26) of the Aeroradiometric measurements. The map shows that the southeast and northwest parts are highly enriched through potassic alteration, characterized by high values associated with *syn*-orogenic granite and metagabbro- diorite. The high values nearly 19.9 marked by pink color are associated with ophiolitic serpentine. It is worth noting that the highly altered southeast region is

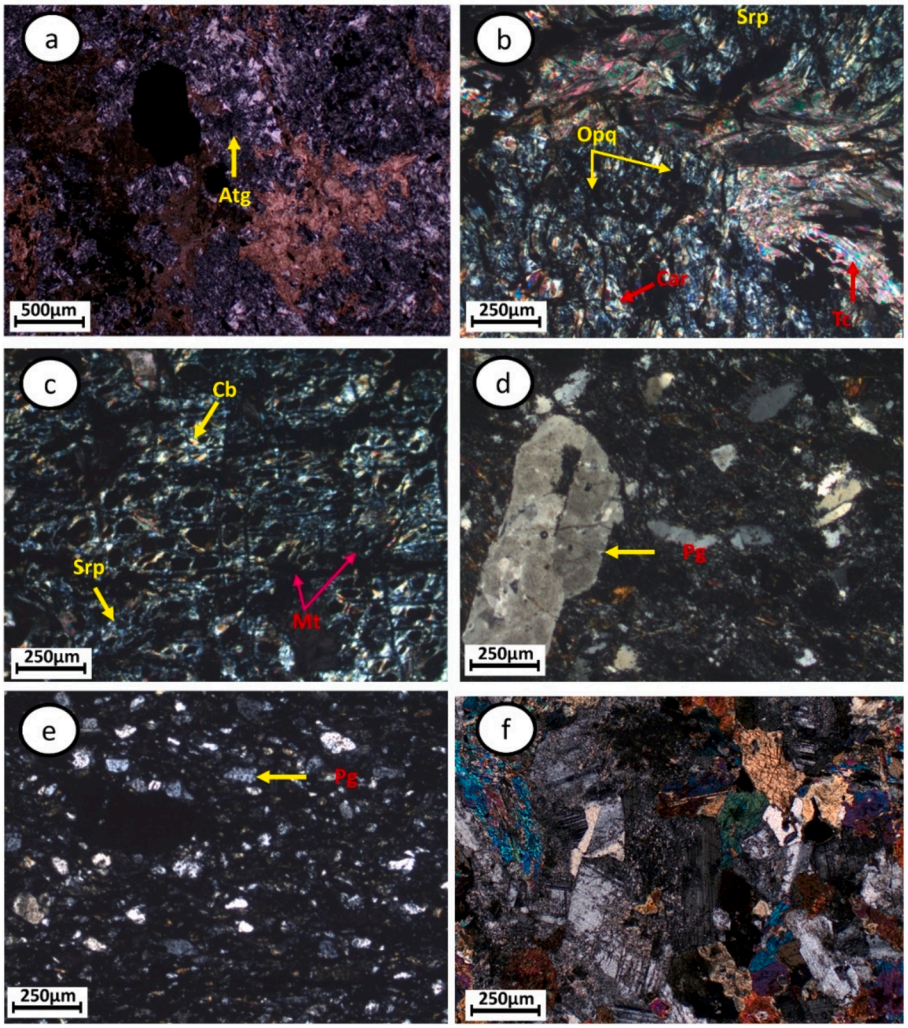

Fig. 29. Photomicrographs showing: a) Bundles of antigorite (Atg) represented by flakes forming the main constituent of serpentinites with occasional replacement of antigorite by carbonates. b) Talc-carbonate (third-order color) associated with serpentinite. c) The pseudomorphic textures, such as mesh serpentine replacements of olivine or pyroxene by antigorite and carbonates, leaving magnetite in the cleavage. d) Metavolcanics displaying a porphyritic texture, consisting of quartz and plagioclase phenocrysts in a groundmass of the same constituents. e) Andesitic metatuffs showing plagioclase with a few quartz crystal fragments embedded in a fine-grained groundmass, and f) Metagabbro-diorite with slightly altered holocrystalline texture. All photos are taken in cross-polarized transmitted light (CN). (Ant: Antigorite, Opq: opaques, Cb: carbonate, Tc: Talc, Mt: Magnetite).

rich in placer deposits as revealed from the analysis of EnMap data. Ultimately, the spawned radioelement ternary composite map (Fig. 26) combines intensities of potassium (K), equivalent thorium (eTh), and equivalent uranium (U) concentrations with red, green, and blue colors respectively. The radiometric response in the ternary map to some extent corresponds with the surface rock units of the study area and shows a fairly close spatial correlation with the rock units presented in geological and EnMap images. High concentrations of K, eTh, and eU radioactive elements are displayed in white color and related to granitoids rocks. They are typically indicated by their strong radiometric response and can be differentiated from the low radioactive rocks. A low concentration of K, eTh, and eU radioactive elements is represented by dark color coincides with ophiolitic serpentine. Nubian Sandstone and wadi deposits are observed in green or blue-green colors. The metagabbro and diorite rocks are shown in pale red color. To sum up, based on these results most of the distinguished lithological units and detected alteration areas are well previously mapped by using EnMap data which confirms their efficiency for the desired target.

5. Verification through field observations and Lab investigations

A field camp was conducted to explore the main lithological and hydrothermal alteration characteristics within the study area. More than 100 field stations were visited, accessible via the wadis crossing the study area. Generally, field investigations confirmed most of our results. For instance, serpentinite, one of the prominent rock units in the study area, was precisely located as identified by EnMap data. Fig. 27a provides a general view of Gabal Um Salatit serpentinite, a prominent serpentinite mountain well-delineated by Fig. 12b. All serpentinite exposures were examined to determine the presence of talc-carbonate associations indicated by remote sensing data. Our field observations revealed dominant talc-carbonate rocks (Fig. 27b and c) in various forms, mostly associated with serpentinites as depicted in Fig. 7a. These blocks are mixed within volcaniclastic metasediments, representing the ophiolitic mélange matrix in the study area (Fig. 27b and c). Additionally, in line with our remote sensing findings (Fig. 7b), intensive deformation was associated with talc-carbonate rocks, indicating thrusting along contacts with other units. Our field investigations

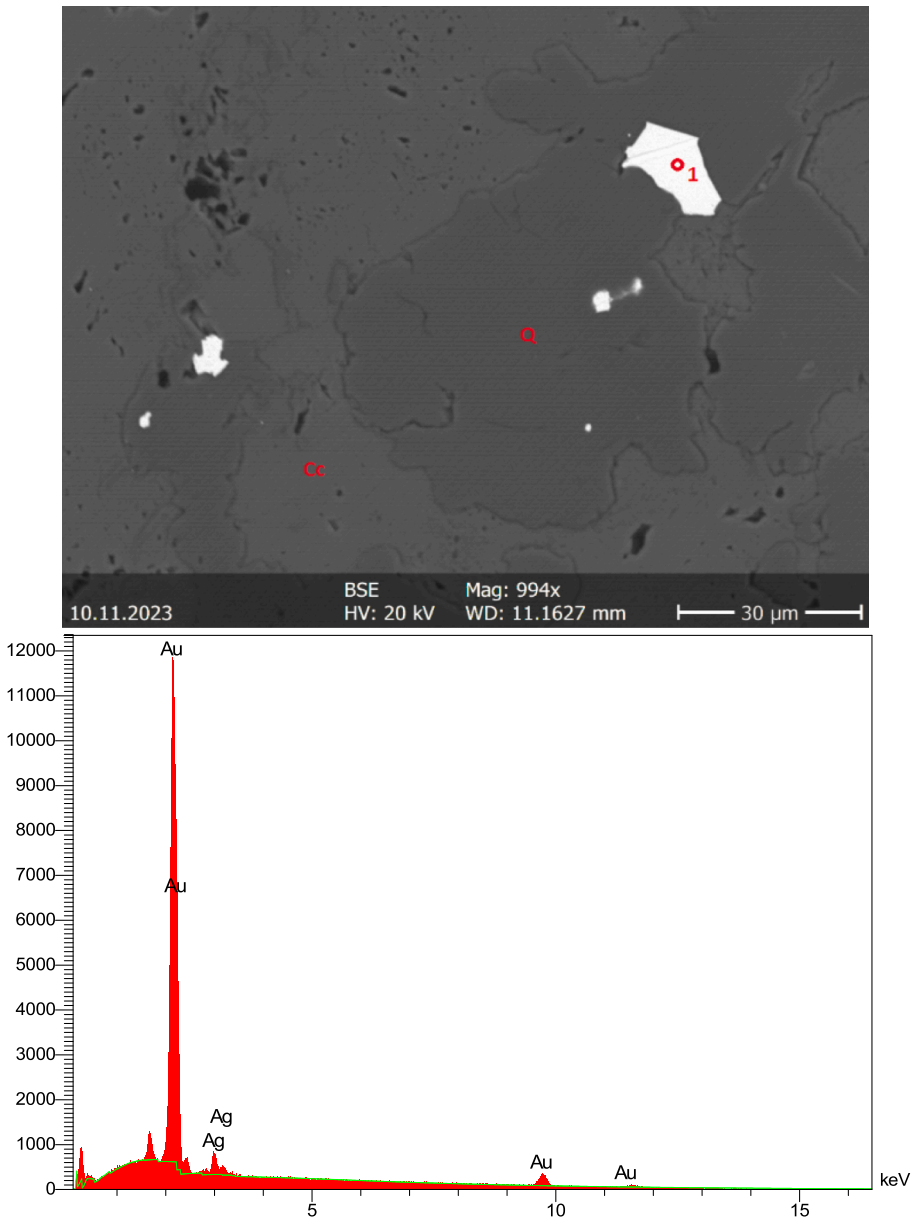

Fig. 30. (a) BSE image and (b) SEM-EDX spectra of electrum (83% gold and 17% silver without any oxygen). Q for quartz, and cc for calcite.

revealed intensively sheared, highly deformed talc carbonate exposures rich in magnesite, as highlighted in Fig. 27d. This deformation and alteration of serpentinite rocks are primarily manifested as listvaenite rocks (Fig. 27e and f).

These deformational events significantly impacted other rock units, notably the metavolcanic rocks (Fig. 28a and b), whose locations precisely matched those indicated in Fig. 13b. The distribution of other rock units, such as metagabbroic rock (Fig. 28c), was thoroughly examined, aligning closely with the indications provided in Fig. 14a. Additionally, granitic rocks were surveyed at various locations (Fig. 28d, e, and f), following the distribution outlined in Fig. 12 a. Our field observations revealed a nearly typical representation of these rocks across the study area. It is essential to highlight that all other remote sensing findings pertaining to chemical compositions or altered zones were meticulously examined. For instance, our investigations corroborated the distribution of Mg-Fe-OH minerals (Fig. 17b) within the serpentinite exposures and Al-OH minerals (Fig. 18a) within the visited granitic rocks.

To strengthen our findings, petrographic investigations were conducted on selected samples to ensure a comprehensive validation of our remote sensing indications. Microscopic analysis of serpentinites (Fig. 29a) highlighted the predominance of antigorite, corroborating the results obtained from our spectral analysis (Fig. 19a), which highlighted the prevalence of antigorite over lizardite and chrysotile. Additionally, talc and carbonates (mainly calcite) were discerned under the microscope (Fig. 29b and c), closely associated with serpentinite, thus affirming our earlier interpretations. Furthermore, examination of acidic metavolcanics (Fig. 29d and e), characterized by metarhyolite, and intermediate metavolcanics, represented by metaandesite, provided further evidence of the intricate nature of metavolcanic formations within the study area. Metagabbro-diorite rocks (Fig. 29f) were also analyzed, revealing a higher mafic content upon microscopic inspection. Further analysis was conducted on the alteration zones identified through EnMap data, confirming the prevalence of clay minerals, quartz, and calcite.

Quartz vein samples were examined using SEM-EDX (Fig. 30), revealing the presence of gold grains close to these identified alteration zones. This assertion is further supported by the identification of the matrix surrounding these gold grains as a quartz-carbonate (calcite)

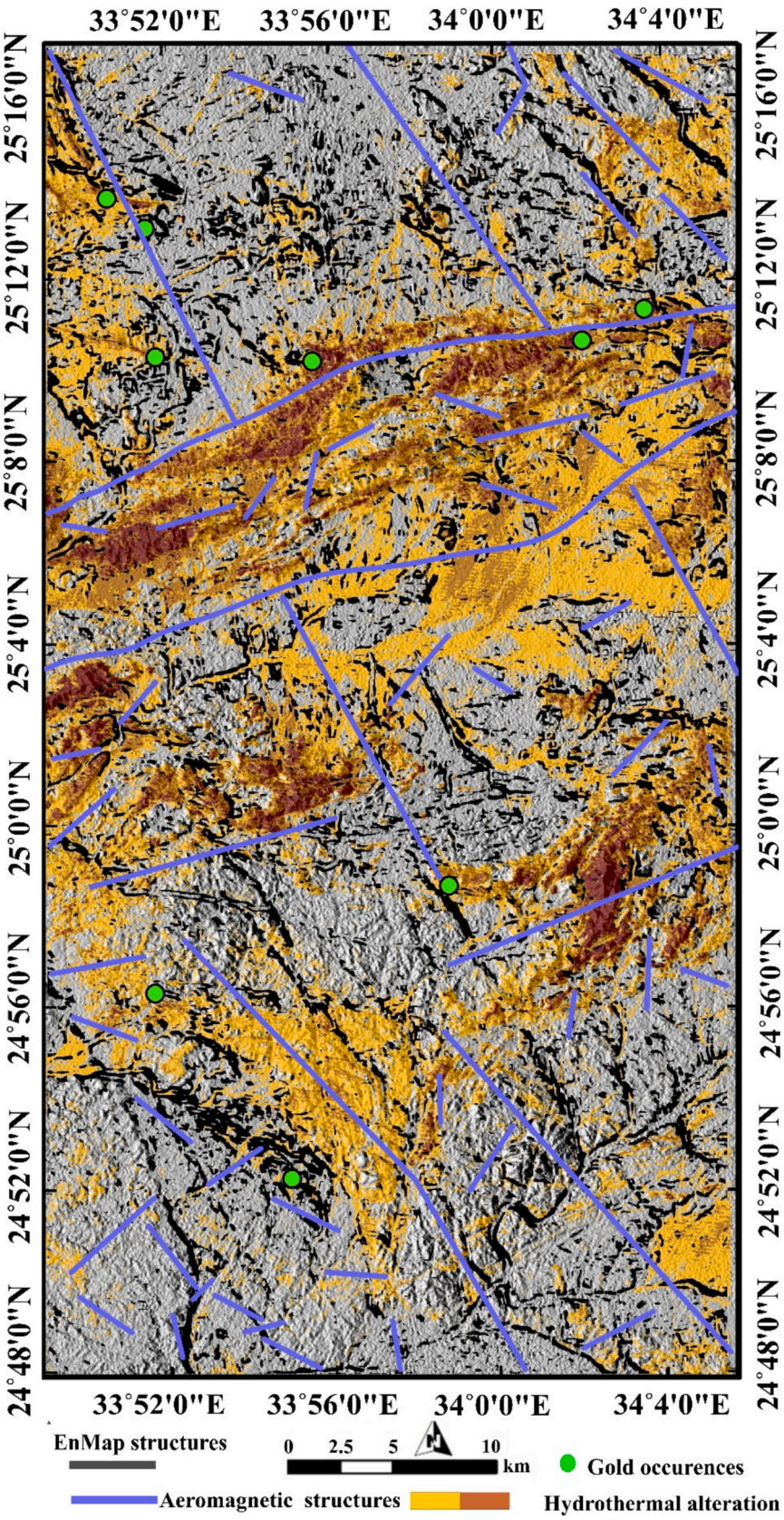

Fig. 31. Spatial overlay analysis showing structures detected via EnMap textural analysis (black), main structures derived from aeromagnetic data (blue), and hydrothermal alteration zones (brown). The alignment of NW-trending structures from both data sources is evident, with heavily dissected areas often coinciding with altered zones. These findings are validated by known gold occurrences (green) in the region. (For interpretation of the references to color in this figure legend, the reader is referred to the web version of this article.)

matrix. These findings strongly support our comprehensive multiscale approach, which integrates EnMap data with airborne geophysical data. While our primary objective was to evaluate the potential of EnMap data for lithological and hydrothermal alteration mapping, these integrated findings were used to develop a simplified gold potentiality map of the study area through a spatial overlay analysis, as presented in Fig. 31. This map highlights the alignment of structures detected by both EnMap and magnetic data, along with hydrothermally altered zones. Collectively, these findings strongly recommend EnMap data as a valuable tool for comprehensive geological analyses and for identifying potential mineralized zones.

Overall, our research indicates that these advancements and the efficiency of EnMAP data are primarily attributed to its enhanced spectral characteristics compared to previous well-known missions. Achieving a signal-to-noise ratio (SNR) of $\geq$ 400:1 in the VNIR and $\geq$ 170:1 in the SWIR represents a significant enhancement, crucial for EnMap. Previous missions, such as Hyperion, faced challenges due to lower signal-to-noise ratios. In contrast, the recently launched Italian PRISMA exhibits improved SNRs of $>$ 160 and $>$ 100 for VNIR and SWIR channels, respectively.

6. Conclusions

The current research evaluated EnMap hyperspectral data in lithological and hydrothermal alteration mapping for a case study located in the Arabian Nubian Shield. Our research integrated airborne geophysical data, field investigation, petrographic analysis, and SEM-EDX measurements to check the results delivered by EnMap data analysis. Our findings indicated a general endorsement of EnMap data for comprehensive lithological and hydrothermal alteration mapping. Our research concluded the following:

1. In such complicated terrains, EnMap data combinations (e.g., FCCs of b224-b118-b3 and b224-b145-b13 in RGB), representations of individual principal and independent components, are efficient in resolving the complexity among lithological units and highlighting their contacts.
2. UMAP confirmed the separability of these lithological features through 2D embeddings, validating the spectral richness of EnMap data and demonstrating the effectiveness of UMAP in distinguishing these lithological characteristics, thus endorsing its utility in future similar applications.
3. Structural insights could be detected through the visual inspections of the distribution of smaller rock units (e.g., talc carbonates), highlighting the ability of EnMap data in both lithological and structural analysis. Furthermore, textural analysis of EnMap data proved highly effective in detecting the main structural features within the study area.
4. SMACC analysis is very effective with EnMap data in setting apart different rock unit abundances and reflecting their spectra as a combined representation of their essential rock-forming minerals. However, some discrepancies in particular absorption features could arise mainly due to the broader pixel size and the contribution of other components due to the complicated history of the study area.
5. Hydrothermal alteration mapping was successfully conducted using EnMap data, revealing pervasive iron-bearing and hydroxyl-bearing alterations within the study area.
6. Spectral correlation of EnMap spectra revealed how well their surface reflectance data is efficient in diagnostic identification in the study area.
7. Geophysical investigations have revealed that gradient approaches of aeromagnetic data are very effective in delineating structural features which serve as channels for hydrothermal alteration. Further, gamma-ray data analysis can effectively differentiate the primary lithological units based on their radiometric content, aligning closely with the lithological boundaries identified by EnMap data, endorsing both of them and their integration.
8. Gold grains were found through SEM-EDX analysis within the zones identified by EnMAP data as hydrothermally altered zones. Additionally, the study highlighted the main placer deposits distribution within the study area, showing spatial proximity to older gold mines.
9. The study developed a potential map for mineralized zones by integrating structural and hydrothermal analyses. It also highlighted the potential presence of bauxite ore in the southwestern corner of the study area, located along the boundary between Nubian sandstone and basement rocks. We strongly recommend further exploration of this region due to the abundance of iron and aluminum-rich rocks.

CRediT authorship contribution statement

Ali Shebl: Writing – review & editing, Writing – original draft, Visualization, Validation, Methodology, Investigation, Formal analysis, Conceptualization. **Mahmoud Abdellatif:** Methodology, Data curation. **Dávid Abriha:** Writing – review & editing, Visualization, Validation, Supervision, Methodology. **Maher Dawoud:** Resources, Investigation. **Mosaad Ali Hussein Ali:** Resources, Methodology, Data curation. **Abdelhalim S. Mahmoud:** Methodology, Investigation. **Ferenc Kristály:** Methodology, Investigation, Data curation. **Árpád Csámer:** Writing – review & editing, Validation, Supervision, Methodology, Investigation, Formal analysis.

Funding

Open access funding provided by University of Debrecen.

Data availability

The datasets used and/or analyzed during the current study are available from the corresponding author upon reasonable request.

Declaration of competing interest

The authors declare that they have no known competing financial interests or personal relationships that could have appeared to influence the work reported in this paper.

Acknowledgements

Great thanks to EnMap organisation for providing the data. Ali Shebl is funded by the Stipendium Hungaricum scholarship under the joint executive program between Hungary and Egypt. Dávid Abriha was supported by the research project NKFI K138079.

References

Abd El-Wahed, M., Attia, M., 2023. Structural and tectonic evolution of suture-related belts and post-accretionary systems in the Arabian-Nubian Shield. Geol. J. 58, 1776–1809.

Abd El-Wahed, M., Attia, M., 2022. Genesis of the gneissic core complexes in the Arabian-Nubian Shield and its tectonic implications: a regional overview. J. Asian Earth Sci. 236, 105337.

Abd El-Wahed, M., Hamimi, Z., 2021. The Egyptian nubian shield within the frame of the arabian–nubian shield. Geol. Egypt. Nubian Shield 15–51.

Abd El-Wahed, M., Kamh, S., Ashmawy, M., Shebl, A., 2019. Transpressive structures in the Ghadir shear belt, eastern desert, Egypt: evidence for partitioning of oblique convergence in the Arabian-Nubian shield during Gondwana agglutination. Acta Geol. Sin. - English Ed. 93, 1614–1646. https://doi.org/10.1111/1755-6724.13882.

Abdel-Karim, A.M., El-Mahallawi, M.M., Finger, F., 1996. The ophiolite mélange of Wadi Dunqash and Arayis, Eastern Desert of Egypt: Petrogenesis and tectonic evolution. Acta Miner Petrogr, Szeged 37, 129–141.

Abdelkader, M.A., Watanabe, Y., Shebl, A., Badawi, M., Dawoud, M., El-Dokouny, H.A., Csámer, Á., Abdellatif, M., 2024. Advanced exploration of rare metal mineralization through integrated remote sensing and geophysical analysis of structurally-

controlled hydrothermal alterations. J. Geochemical Explor. 267, 107598. https://doi.org/10.1016/j.gexplo.2024.107598.
Abdelkader, M.A., Watanabe, Y., Shebl, A., El-Dokouny, H.A., Dawoud, M., Csámer, Á., 2022. Effective delineation of rare metal-bearing granites from remote sensing data using machine learning methods: a case study from the Umm Naggat Area, Central Eastern Desert Egypt. Ore Geol. Rev. 150, 105184. https://doi.org/10.1016/J.OREGEOREV.2022.105184.
Abdelsalam, M.G., Stern, R.J., 1996. Sutures and shear zones in the Arabian-Nubian Shield. J. African Earth Sci. 23, 289–310.
Adiri, Z., Lhissou, R., El Harti, A., Jellouli, A., Chakouri, M., 2020. Recent advances in the use of public domain satellite imagery for mineral exploration: a review of Landsat-8 and Sentinel-2 applications. Ore Geol. Rev. 117, 103332. https://doi.org/10.1016/j.oregeorev.2020.103332.
Aero-Service, 1984. Final operational report of airborne magnetic/radiation survey in the Eastern Desert, Egypt. For the Egyptian General Petroleum Corporation (EGPC) and the Egyptian Geological Survey and Mining Authority (EGSMA).
Afolabi, D.O., Akinlalu, A.A., Sanusi, S.O., 2024. Integrated geophysical and remote sensing investigations in hydrothermal mapping for orogenic gold mineralization in parts of Ife–Ilesa schist belt SW Nigeria—a case study. Arab. J. Geosci. 17, 244. https://doi.org/10.1007/s12517-024-12048-6.
Aggarwal, A., Garg, R.D., 2015. Systematic approach towards extracting endmember spectra from hyperspectral image using PPI and SMACC and its evaluation using spectral library. Appl. Geomatics 7, 37–48. https://doi.org/10.1007/s12518-014-0149-5.
Ahmed, A.H., 2022. Mineral Deposits and Occurrences in the Arabian-Nubian Shield. Springer Nature.
Amigun, J.O., Sanusi, S.O., Audu, L., 2022. Geophysical characterisation of rare earth element and gemstone mineralisation in the Ijero-Aramoko pegmatite field, southwestern Nigeria. J. African Earth Sci. 188, 104494. https://doi.org/10.1016/j.jafrearsci.2022.104494.
Amin, M.S., 1954. The ilmenite deposit of Abu Ghalqa Egypt. Econ. Geol. 49, 77–87.
Bachmann, M., Alonso, K., Carmona, E., Gerasch, B., Habermeyer, M., Holzwarth, S., Krawczyk, H., Langheinrich, M., Marshall, D., Pato, M., Pinnel, N., de losReyes, R., Schneider, M., Schwind, P., Storch, T., 2021. Analysis-ready data from hyperspectral sensors—the design of the EnMAP CARD4L-SR data product. Remote Sens. 13. https://doi.org/10.3390/rs13224536.
Badawi, M., Abdelatif, M., Shebl, A., Makroum, F., Shalaby, A., Nemeth, N., 2022. Mapping Structurally Controlled Alterations Sparked by Hydrothermal Activity in the Fatira-Abu Zawal Area, Eastern Desert, Egypt. Acta Geol. Sin. - English Ed. https://doi.org/10.1111/1755-6724.15019.
Balázs, B., Bíró, T., Dyke, G., Singh, S.K., Szabó, S., 2018. Extracting water-related features using reflectance data and principal component analysis of Landsat images. Hydrol. Sci. J. 63, 269–284.
Basta, E.Z., Takla, M.A., 1968. Petrological studies on Abu Ghalaga ilmenite occurrence, Eastern Desert. J. Geol. 12, 43–72.
Bedini, E., Chen, J., 2022. Application of PRISMA satellite hyperspectral imagery to mineral alteration mapping at Cuprite, Nevada, USA. J. Hyperspectral Remote Sens. 124–130.
Bioucas-Dias, J.M., Plaza, A., Camps-Valls, G., Scheunders, P., Nasrabadi, N., Chanussot, J., 2013. Hyperspectral remote sensing data analysis and future challenges. IEEE Geosci. Remote Sens. Mag. 1, 6–36. https://doi.org/10.1109/MGRS.2013.2244672.
Bishop, J.L., 2019. Visible and Near-Infrared Reflectance Spectroscopy: Laboratory Spectra of Geologic Materials. In: Bishop, J.L., Bell III, J.F., Moersch, J.E.E. (Eds.), Remote Compositional Analysis: Techniques for Understanding Spectroscopy, Mineralogy, and Geochemistry of Planetary Surfaces, Cambridge Planetary Science. Cambridge University Press, pp. 68–101.
Blakely, R.J., Simpson, R.W., 1986. Approximating edges of source bodies from magnetic or gravity anomalies. Geophysics 51, 1494–1498.
Colin V. Reeves, and P.W.Z., 1990. Airborne geophysics and remote sensing: some common ground in presentation techniques and interpretation. Remote Sens. an Oper. Technol. Min. Pet. Ind. 75–88.
Cordell, L., Grauch, V.J.S., 1985. Mapping basement magnetization zones from aeromagnetic data in the San Juan Basin, New Mexico, In: The Utility of Regional Gravity and Magnetic Anomaly Maps. Society of Exploration Geophysicists, pp. 181–197.
Darnley, A.G., Grasty, R.L., Charbonneau, B.W., 1970. HIGHLIGHTS OF GSC AIRBORNE GAMMA SPECTROMETRY IN 1969.
Devi, M.R.V., Kalaivani, S., 2023. Endmember estimation using fuzzy grade of membership and spectral matching. IEEE Access.
Douglas, A., Kereszturi, G., Schaefer, L.N., Kennedy, B., 2022. Rock alteration mapping in and around fossil shallow intrusions at Mt. Ruapehu New Zealand with laboratory and aerial hyperspectral imaging. J. Volcanol. Geoth. Res. 432, 107700.
Duval, J.S., 1983. Composite color images of aerial gamma-ray spectrometric data. Geophysics 48, 722–735.
Efimov, A.V., 1978. Multiplikativnyj pokazatel dlja vydelenija endogennych rud poaerogamma-spektrometriceskim dannym. Rudn. Geofiz. Leningrad, Naucn. objedinenie Geofiz, Metod.
El-Ramly, M.F., 1984. On tectonic evolution of the Wadi Hafafit area and environs, Eastern Desert of Egypt. Fac. Earth Sci. King Abdulaziz Univ. Bull. 6, 113–126.
El-Shazly, E.M., 1959. Report on the Ilmenite Ore at Abu Ghalaga Eastern Desert. Unpubl, Rep.
El Kazzaz, Y.A., 2012. Shear zones related gold-bearing quartz veins in Shinai area, South Eastern Desert. Egypt. Egypt. J. Geol. 56, 67–89.
Elkhateeb, S.O., Abdellatif, M.A.G., 2018. Delineation potential gold mineralization zones in a part of Central Eastern Desert, Egypt using Airborne Magnetic and Radiometric data. NRIAG J. Astron. Geophys. 7, 361–376.
Fowler, A.-R., El Kalioubi, B., 2002. The Migif-Hafafit gneissic complex of the Egyptian Eastern Desert: fold interference patterns involving multiply deformed sheath folds. Tectonophysics 346, 247–275.
Fowler, A., Osman, A.F., 2009. The Sha'it–Nugrus shear zone separating Central and South Eastern Deserts, Egypt: a post-arc collision low-angle normal ductile shear zone. J. African Earth Sci. 53, 16–32.
Goetz, A.F.H., Vane, G., Solomon, J.E., Rock, B.N., 1985. Imaging spectrometry for earth remote sensing. Science (80-) 228, 1147–1153. https://doi.org/10.1126/science.228.4704.1147.
Greiling, R.O., Abdeen, M.M., Dardir, A.A., El Akhal, H., El Ramly, M.F., El Din Kamal, G. M., Osman, A.F., Rashwan, A.A., Rice, A.H.N., Sadek, M.F., 1994. A structural synthesis of the Proterozoic Arabian-Nubian Shield in Egypt. Geol. Rundschau 1994 833 83, 484–501. https://doi.org/10.1007/BF01083222.
Hamimi, Z., Abd El-Wahed, M.A., 2020. Suture (s) and major shear zones in the Neoproterozoic basement of Egypt. Geol. Egypt 153–189.
Hamimi, Z., El-Fakharani, A., Emam, A., Barreiro, J.G., Abdelrahman, E., Abo-Soliman, M.Y., 2018. Reappraisal of the kinematic history of Nugrus shear zone using PALSAR and microstructural data: implications for the tectonic evolution of the Eastern Desert tectonic terrane, northern Nubian Shield. Arab. J. Geosci. 11, 1–29.
Hamimi, Z., Fowler, A.-R., Liégeois, J.-P., Collins, A., Abdelsalam, M.G., Abd El-Wahed, M., 2021. The geology of the Arabian-Nubian shield. Springer.
Harris, J.R., Ford, K.L., Charbonneau, B.W., 2009. Application of gamma-ray spectrometer data for lithological mapping in a cordilleran environment, Sekwi Region. NWT. Can. J. Remote Sens. 35, S12–S30.
Johnson, P.R., Woldehaimanot, B., 2003. Development of the Arabian-Nubian Shield: perspectives on accretion and deformation in the northern East African Orogen and the assembly of Gondwana. Geol. Soc. London Spec. Publ. 206, 289–325.
Khedr, M.Z., Al Desouky, A.A., Kamh, S., Hauzenberger, C., Arai, S., Tamura, A., Whattam, S.A., Morishita, T., Lasheen, E.S.R., El-Awady, A., 2023. Petrogenesis of Gerf Neoproterozoic carbonatized peridotites (Egypt): evidence of convergent margin metasomatism of depleted sub-arc mantle. Lithos 450–451, 107192. https://doi.org/10.1016/J.LITHOS.2023.107192.
Kumar, C., Chatterjee, S., Oommen, T., Guha, A., 2020. Automated lithological mapping by integrating spectral enhancement techniques and machine learning algorithms using AVIRIS-NG hyperspectral data in Gold-bearing granite-greenstone rocks in Hutti, India. Int. J. Appl. Earth Obs. Geoinf. 86, 102006. https://doi.org/10.1016/J.JAG.2019.102006.
Kusky, T., Wang, J., Wang, L., Huang, B., Ning, W., Fu, D., Peng, H., Deng, H., Polat, A., Zhong, Y., Shi, G., 2020. Mélanges through time: life cycle of the world's largest Archean mélange compared with Mesozoic and Paleozoic subduction-accretion-collision mélanges. Earth-Sci. Rev. https://doi.org/10.1016/j.earscirev.2020.103303.
Kusky, T.M., Bradley, D.C., 1999. Kinematic analysis of mélange fabrics: examples and applications from the McHugh Complex, Kenai Peninsula. Alaska. J. Struct. Geol. 21, 1773–1796.
Lekka, C., Petropoulos, G.P., Detsikas, S.E., 2024. Appraisal of EnMAP hyperspectral imagery use in LULC mapping when combined with machine learning pixel-based classifiers. Environ Model Softw. 173, 105956. https://doi.org/10.1016/j.envsoft.2024.105956.
McInnes, L., Healy, J., Melville, J., 2018. Umap: Uniform manifold approximation and projection for dimension reduction. arXiv Prepr. arXiv1802.03426.
Miller, H.G., Singh, V., 1994. Potential field tilt—a new concept for location of potential field sources. J. Appl. Geophys. 32, 213–217.
Mostafa, R., Hagag, W., Hamimi, Z., Fowler, A.-R., El-Hemaly, I., 2022. Paleomagnetism as a geochronological gauge for deformational events: Insights from the Najd-related Nugrus Shear Zone, Northern Nubian Shield. J. Asian Earth Sci. 223, 104988.
Myasnikov, E., 2020. Using UMAP for dimensionality reduction of hyperspectral data, In: 2020 International Multi-Conference on Industrial Engineering and Modern Technologies (FarEastCon). pp. 1–5.
Nabighian, M.N., 1974. Additional comments on the analytic signal of two-dimensional magnetic bodies with polygonal cross-section. Geophysics 39, 85–92.
Ostrovskiy, E.Y., 1975. Antagonism of radioactive elements in wallrock alterations fields and its use in aerogamma spectrometric prospecting. Int. Geol. Rev. 17, 461–468.
Roger, J., Irakulis-Loitxate, I., Valverde, A., Gorroño, J., Chabrillat, S., Brell, M., Guanter, L., 2024. High-resolution methane mapping with the EnMAP satellite imaging spectroscopy mission. IEEE Trans. Geosci. Remote Sens. 62, 1–12. https://doi.org/10.1109/TGRS.2024.3352403.
Sabins, F.F., 1999. Remote sensing for mineral exploration. Ore Geol. Rev. 14, 157–183. https://doi.org/10.1016/S0169-1368(99)00007-4.
Sanusi, S.O., Amigun, J.O., 2020a. Structural and hydrothermal alteration mapping related to orogenic gold mineralization in part of Kushaka schist belt, North-central Nigeria, using airborne magnetic and gamma-ray spectrometry data. SN Appl. Sci. 2, 1–26.
Sanusi, S.O., Amigun, J.O., 2020b. Logistic-based translation of orogenic gold forming processes into Mappable exploration criteria for fuzzy logic mineral exploration targeting in the Kushaka Schist Belt, North-Central Nigeria. Nat. Resour. Res. 29, 3505–3526. https://doi.org/10.1007/s11053-020-09689-1.
Sanusi, S.O., Josiah, D.-I.-A., Olaniyan, O., Olayanju, G.M., 2024a. Delineation of Potential Gold Mineralization Zones in the Kushaka Schist Belt, Northcentral Nigeria, Using Geochemical, Ground Magnetic, Induced Polarization, and Electrical Resistivity Methods. Mining Metall. Explor. 41, 2007–2029. https://doi.org/10.1007/s42461-024-01033-y.

Sanusi, S.O., Olaniyan, O., Afolabi, D.O., Olayanju, G.M., 2024b. Mapping of orogenic gold mineralization potential in the Kushaka Schist Belt, Northcentral Nigeria: insights from point pattern, Kernel density, staged-factor, and fuzzy AHP modeling techniques. Earth Syst. Environ. https://doi.org/10.1007/s41748-024-00427-8.

Savitri, K.P., Hecker, C., van der Meer, F.D., Sidik, R.P., 2021. VNIR-SWIR infrared (imaging) spectroscopy for geothermal exploration: current status and future directions. Geothermics 96, 102178. https://doi.org/10.1016/j.geothermics.2021.102178.

Schmitz, S., Weidner, U., Hammer, H., Thiele, A., 2021. Evaluating uniform manifold approximation and projection for dimension reduction and visualization of PolInSAR features. ISPRS Ann. Photogramm. Remote Sens. Spat. Inf. Sci. 1, 39–46.

Shackleton, R., 1988. Contrasting structural relationships of Proterozoic ophiolites in Northeast and Eastern Africa. Contrasting Struct. relationships Proterozoic ophiolites Northeast East, Africa.

Shebl, A., Abdellatif, M., Badawi, M., Dawoud, M., Fahil, A.S., Csámer, Á., 2023a. Towards better delineation of hydrothermal alterations via multi-sensor remote sensing and airborne geophysical data. Sci. Rep. 13, 7406.

Shebl, A., Abdellatif, M., Elkhateeb, S.O., Csámer, Á., 2021a. Multisource Data Analysis for Gold Potentiality Mapping of Atalla Area and Its Environs, Central Eastern Desert, Egypt. Miner. 2021, Vol. 11, Page 641 11, 641. https://doi.org/10.3390/MIN11060641.

Shebl, A., Abriha, D., Fahil, A.S., El-Dokouny, H.A., Elrasheed, A.A., Csámer, Á., 2023b. PRISMA hyperspectral data for lithological mapping in the Egyptian Eastern Desert: evaluating the support vector machine, random forest, and XG boost machine learning algorithms. Ore Geol. Rev., 105652

Shebl, A., Csámer, Á., 2021a. Reappraisal of DEMs, Radar and optical datasets in lineaments extraction with emphasis on the spatial context. Remote Sens. Appl.: Soc. Environ. 24, 100617. https://doi.org/10.1016/J.RSASE.2021.100617.

Shebl, A., Csámer, Á., 2021b. Lithological, structural and hydrothermal alteration mapping utilizing remote sensing datasets: a case study around Um Salim area. Egypt. IOP Conf. Ser. Earth Environ. Sci. 942, 012032. https://doi.org/10.1088/1755-1315/942/1/012032.

Shebl, A., Kusky, T., Csámer, Á., 2022. Advanced land imager superiority in lithological classification utilizing machine learning algorithms. Arab. J. Geosci. 159 (15), 1–13. https://doi.org/10.1007/S12517-022-09948-W.

Shereif, A.S., Shebl, A., Mahmoud, A.S., Csámer, Á., 2024. Enhanced lithological mapping in El-Missikat and El-Erediya Areas, Central Eastern Desert, Egypt, leveraging remote sensing techniques and machine learning algorithms. IEEE Trans. Geosci. Remote Sens. 62, 1–27. https://doi.org/10.1109/TGRS.2024.3471982.

Simpson, M.P., Rae, A.J., 2018. Short-wave infrared (SWIR) reflectance spectrometric characterisation of clays from geothermal systems of the Taupō Volcanic Zone, New Zealand. Geothermics 73, 74–90. https://doi.org/10.1016/j.geothermics.2018.01.006.

Singh, P., Pandey, P.C., Petropoulos, G.P., Pavlides, A., Srivastava, P.K., Koutsias, N., Deng, K.A.K., Bao, Y., 2020. 8 - Hyperspectral remote sensing in precision agriculture: present status, challenges, and future trends. In: Pandey, P.C., Srivastava, P.K., Balzter, H., Bhattacharya, B., Petropoulos, G.P. (Eds.), Hyperspectral Remote Sensing. Elsevier, Earth Observation, pp. 121–146. https://doi.org/10.1016/B978-0-08-102894-0.00009-7.

Stern, R.J., 1994. Arc-assembly and continental collision in the Neoproterozoic African orogen: implications for the consolidation of Gondwanaland. Annu. Rev. Earth Planet. Sci. 22, 319–351.

Stern, R.J., Johnson, P.R., Kröner, A., Yibas, B., 2004. Neoproterozoic ophiolites of the Arabian-Nubian shield. Dev. Precambrian Geol. 13, 95–128.

Storch, T., Honold, H.-P., Chabrillat, S., Habermeyer, M., Tucker, P., Brell, M., Ohndorf, A., Wirth, K., Betz, M., Kuchler, M., Mühle, H., Carmona, E., Baur, S., Mücke, M., Löw, S., Schulze, D., Zimmermann, S., Lenzen, C., Wiesner, S., Aida, S., Kahle, R., Willburger, P., Hartung, S., Dietrich, D., Plesia, N., Tegler, M., Schork, K., Alonso, K., Marshall, D., Gerasch, B., Schwind, P., Pato, M., Schneider, M., de los Reyes, R., Langheinrich, M., Wenzel, J., Bachmann, M., Holzwarth, S., Pinnel, N., Guanter, L., Segl, K., Scheffler, D., Foerster, S., Bohn, N., Bracher, A., Soppa, M.A., Gascon, F., Green, R., Kokaly, R., Moreno, J., Ong, C., Sornig, M., Wernitz, R., Bagschik, K., Reintsema, D., La Porta, L., Schickling, A., Fischer, S., 2023. The EnMAP imaging spectroscopy mission towards operations. Remote Sens. Environ. 294, 113632. https://doi.org/https://doi.org/10.1016/j.rse.2023.113632.

van der Meer, F., Kopačková, V., Koucká, L., van der Werff, H.M.A., van Ruitenbeek, F.J.A., Bakker, W.H., 2018. Wavelength feature mapping as a proxy to mineral chemistry for investigating geologic systems: an example from the Rodalquilar epithermal system. Int. J. Appl. Earth Obs. Geoinf. 64, 237–248. https://doi.org/10.1016/j.jag.2017.09.008.

Zoheir, B., El-Wahed, M.A., Pour, A.B., Abdelnasser, A., 2019. Orogenic gold in transpression and transtension zones: field and remote sensing studies of the barramiya–mueilha sector. Egypt. Remote Sens. 11, 2122.

Zoheir, B., Lehmann, B., 2011. Listvenite–lode association at the Barramiya gold mine, Eastern Desert Egypt. Ore Geol. Rev. 39, 101–115. https://doi.org/10.1016/J.OREGEOREV.2010.12.002.

Zoheir, B., Weihed, P., 2014. Greenstone-hosted lode-gold mineralization at Dungash mine, Eastern Desert Egypt. J. African Earth Sci. 99, 165–187.